Journal Pre-proof

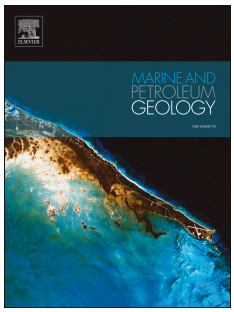

Evaluating the sedimentological and diagenetic impacts on terrestrial lacustrine fan delta sandy conglomerates reservoir quality: Insights from the Triassic Baikouquan Formation in the Mahu sag, Junggar Basin, Western China

Zhichao Yu, Zhizhang Wang, Wentian Fan, Jie Wang, Ziyan Li

PII: S0264-8172(22)00451-2

DOI: https://doi.org/10.1016/j.marpetgeo.2022.105973

Reference: JMPG 105973

To appear in: *Marine and Petroleum Geology*

Received Date: 21 April 2022

Revised Date: 4 October 2022

Accepted Date: 10 October 2022

Please cite this article as: Yu, Z., Wang, Z., Fan, W., Wang, J., Li, Z., Evaluating the sedimentological and diagenetic impacts on terrestrial lacustrine fan delta sandy conglomerates reservoir quality: Insights from the Triassic Baikouquan Formation in the Mahu sag, Junggar Basin, Western China, *Marine and Petroleum Geology* (2022), doi: https://doi.org/10.1016/j.marpetgeo.2022.105973.

Evaluating the sedimentological and diagenetic impacts on terrestrial lacustrine fan delta sandy conglomerates reservoir quality: Insights from the Triassic Baikouquan Formation in the Mahu sag, Junggar Basin, Western China.

Zhichao Yu [a], Zhizhang Wang [a,*], Wentian Fan [a], Jie Wang [b], Ziyan Li [a].

[a.] *College of Geosciences, China University of Petroleum, Beijing 102249, China.*

[b.] *CNOOC China Limited, Shenzhen Branch, Shenzhen, Guangdong 518064, China.*

∗ *Corresponding author.*

E-mail address: wang_zhizhang@126.com (Z. Wang).

ABSTRACT

The terrestrial lacustrine fan delta conglomerate reservoirs in the Triassic Baikouquan Formation (BF) are the primary hydrocarbon exploration targets in the Mahu sag, Junggar Basin, Western China. However, the varying lithofacies and complex diagenesis controlling the reservoir quality remain poorly understood. For the sake of revealing how reservoir quality is associated with sedimentary processes and diagenetic alterations, we used integrated approaches like petrographical analysis, cores description, wireline, X-ray diffraction (XRD), scanning electron microscopy (SEM), mercury intrusion capillary pressure (MICP) and measured petrophysical properties. The results showed that sedimentary processes have considerable control over facies distribution, grain size, and clay content, causing spatial variation of reservoir quality within the fan delta deposits. The coarser grain and high clay content fraction at the base of gravity flow will first settle in the fan delta plain near provenance, whereas the finer grains at the top of flows progressively deposit in the fan delta front areas. From proximal to distal fan delta, a progressive conversion from cohesive muddy debris flow into traction current can be inferred from the variations of lithofacies associations. A total of 8 types of microfacies were identified where the conglomerates of the BF were deposited. The

grayish-green fine-grained conglomerates concentrated in the subaqueous distributary channels provide the best reservoir performance, whereas debris flow deposits dominated primarily by muddy debrites occupy the worst reservoir quality because of their highest clay content and coarsest grain size.

The dominant diagenetic events include mechanical compaction that continued throughout the entire burial, two phases of quartz cementation, dissolution of unstable components, early and late carbonate cementation, precipitation of authigenic clay minerals, and two phases of hydrocarbon charging. It is unveiled that compaction is the predominant mechanism negatively affecting reservoir quality in the fan delta complex, while the effect of cementation on pore reduction of the conglomerate reservoir is weaker than compaction. Simultaneously, a complex relationship exists between reservoir petrophysical properties within different clay minerals. Dissolution does not significantly improve the permeability of the reservoir because of the partial dissolution which primarily generated intragranular pores with strong heterogeneity and poor connectivity. The most favorable reservoirs occur primarily in the subaqueous distributary channels in the fan delta front, which comprise well-sorted fine-grained conglomerates with well-developed residual intergranular pores and secondary dissolution pores and have undergone two phases of oil charge. This work may provide a useful reference for hydrocarbon exploration of the fan delta systems and regions which have encountered similar sedimentary and diagenetic processes.

Keywords: Lacustrine fan delta; Conglomerate reservoirs; Sedimentary lithofacies; Diagenesis; Reservoir quality.

1. Introduction

Fan delta reservoirs have grown in importance as locations for petroleum development over the last few decades. Numerous study efforts have been made into such deposits globally ever since Holmes' original proposal in 1965. It could be defined as a type of coarse-grained sedimentary system deposited at the junction of an active fan body and stable water (ocean or lake) with the alluvial fan as provenance. The complex displays the characteristics of rapid

accumulation with near-source, strong heterogeneity, laterally abrupt lithofacies variation, and thick sediments (Xun et al., 2019; Tang et al., 2017). The size and nature of the fan delta vary depending on the radii (or longitudinal extension distance), which are typically in the range of tens of meters to thousands of meters, with a maximum radius of more than tens of kilometers. (Jiang et al., 2020; Jia et al., 2016). Due to their unique structural background (such as adjacent to faults) and the characteristic of rapid accumulation, the fan delta deposits ordinarily occur as wedge-shaped sedimentary bodies with a radius of several kilometers and an area of tens of square kilometers. The sediments are coarse-grained, poorly sorted, and contain much clay matrix. Currently, few large-scale fan deltas have been unearthed owing to the fact that a favorable combination of various geological conditions is required to form such a sedimentary system (Xiao et al., 2021). So far, the only example of a large-scale marine fan delta is the Sant Llorente Munt fan delta dating back to the middle Eocene in the Ebro basin, northern Mediterranean, with an extension distance of about 20 km (Paccard et al., 2012). Similarly, large lacustrine fan deltas are only present in the slope belt of the Mahu Sag of the Junggar Basin in China, including the Xiazijie fan, Huangyangquan fan, and Karamay fan (Tang et al., 2021; Lu et al., 2019). They are substantially larger than the delta of the aforementioned marine fan delta, with a longitudinal radius of 40–45 km. Unlike the fan delta that evolved in a marine environment, the lacustrine fan delta is only marginally altered by waves and tides, thus making its internal sedimentary characteristics well preserved and forming large-scale lithological reservoirs (Xu et al., 2019).

Assessment of reservoir quality is crucial for identifying the distribution of advantageous “sweet spots” in conglomerate reservoirs and has a significant impact on hydrocarbon exploitation. In contrast with traditional sandstone reservoirs, conglomerate reservoirs display distinct lithofacies and complicated diagenesis (Ehrenberg et al., 2019; Guo et al., 2021; Wilson et al., 2020). Hence, the reservoirs present substantial heterogeneity and the formation mechanism of the sweet spot remains unclarified, thus restricting the fine and sustainable hydrocarbon development. Generally, both sedimentary environments and diagenetic alteration play a critical role significantly influencing the reservoir quality. The reservoir architecture,

sedimentary microfacies, rock texture, and primary porosity and permeability are initially determined by the sedimentary process (Wheatley et al., 2020; Kra et al., 2022). Nevertheless, the reservoir quality may be enhanced by dissolution or deteriorated by compaction and cementation in later diagenetic processes. Therefore, comprehensively evaluating the role of sedimentation and diagenetic processes in reservoir quality is essential to determine and forecast high-quality reservoirs.

Until now, a great quantity of hydrocarbons has been found and extracted from the Triassic BF in the fan-delta complex. However, the reservoir exhibits the characteristics of abrupt lithology variation, poor physical properties, and complex diagenetic alteration (Wu et al., 2020), which throws obstacles for quantitatively evaluating reservoir potential. Available literature predominantly explicating the primary role of the diagenetic process in reservoir quality in the research area are (1) alkali minerals like calcite and orthoclase underwent remarkable dissolution attributed to acidic hydrocarbon-containing fluid (Zhu et al., 2019; Jin et al., 2017; Zhu et al., 2010) and (2) authigenic minerals were precipitated as cements, involving later-stage calcites, quartz, and clay minerals like kaolinite and chlorite (Xu et al., 2020; Tan et al., 2014). No research has linked the sedimentary process and diagenesis to determine the distribution of the high-quality reservoirs, whereas different lithology has undergone distinct diagenesis. Furthermore, lacustrine fan delta reservoirs and marine fan delta reservoirs differ significantly in terms of their sedimentary environments, reservoir architecture, detrital components, as well as pore water properties. Therefore, linking the sedimentary process and the diagenetic process could help realize a better comprehension to predict the spatiotemporal distribution of the high-quality reservoirs in the Mahu Oilfield. On the foundation of sedimentologic and petrographical analysis, the current study aims to (1) identify the lithofacies and diagenetic minerals via thorough and detailed core and microscopic examination; (2) quantitatively reveal how reservoir quality is associated with the original sedimentary process and subsequent diagenetic alteration; (3) establish the diagenetic evolution model within different lithofacies, thus providing a theoretical foundation for the location of high-quality reservoirs.

2. Geological setting

The Junggar Basin (total area ~$13 \times 10^4 km^2$) is in the northern part of Xinjiang Uygur Autonomous Region, which is the second biggest basin in the PRC (Fig. 1A). This region is a huge intermountain basin surrounded by Paleozoic folded mountains. It is tectonically subdivided into 6 primary structural units and 44 secondary structural units (Feng et al., 2019). The primary structural units include Wulungu Depression, Lujiang Uplift, Central Depression, West Uplift, East Uplift, and North Tianshan Thrust Belt (Fig. 1B). It is a large continental superimposed basin with tectonic activity dating from the late Carboniferous to the Quaternary. In the early and middle Permian, the compression and nappe between the Siberian and Tarim plates contributed to the forming of a continental foreland basin on the northwestern edge of the basin. The basin again witnessed large-scale tectonic activities from the late Permian to the Paleogene, and the foreland basin progressively transformed into a depression basin (Lu et al., 2019). Thereafter, tectonic activity appears to have slowed, and after the Neogene, the strata were deposited intermittently, resulting in the current stratigraphic distribution.

The Mahu Sag (100 km long; 50 km wide) is at the northern edge of the basin, limited in the west by the Kebai and Wuxia fault zones and in the east by the Dabasong and Xiayan uplifts (Fig. 1B). It is a secondary structure unit belonging to the central depression, covering an area of about 6800 km^2. This study focuses on the MA131 well block in the clival area of the northern Mahu Sag (Fig. 1C). The study area is predominated by the Xiazijie fan delta complex, where pre-fan delta facies, fan delta front facies, and fan delta plain facies had developed in a successive manner.

The lower Baikouquan, middle Karamay, and upper Baijiantan formations were deposited within the Mahu Sag during the Triassic period (Fig. 2). The target stratum in this paper is the BF of Lower Triassic, which unconformably overlies the Middle Permian lower Wuerhe Formation (P_2w) and is overlain by the Middle Triassic Karamay Formation (T_2k) (Tang et al., 2018). The BF is dominated by fluvio-lacustrine deposits of conglomerates interbedded with pebbly sand rock, sand rock, and mudstone (Zou et al., 2015). The BF is subdivided into 3 members from bottom to top composed of the 3rd (T_1b_1), the 2nd (T_1b_2), and the 1st member

139 (T_1b_3), respectively. From Mbr 1 to Mbr 3, the retrograded fan deltaic depositional system came
140 into being in the process of lake transgression. Numerous sets of thick glutenite developed
141 vertically, leading to the development of large-scale high-quality lithologic reservoirs (Zou et
142 al., 2017; Yao et al., 2017).

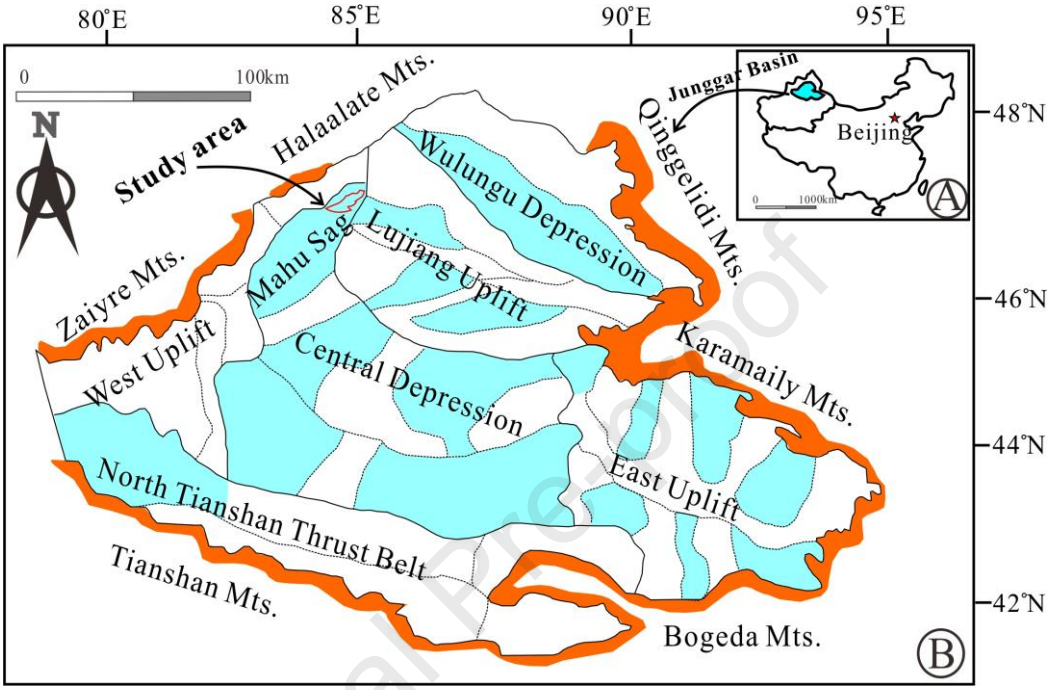

143

144

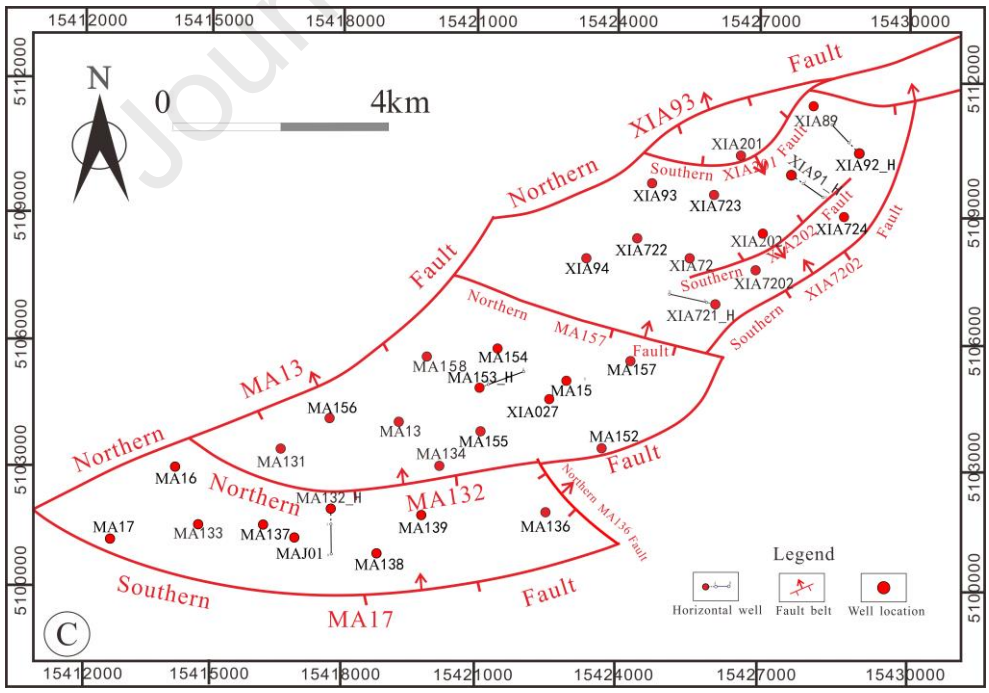

145

146 **Fig. 1. (A) The map showing where the Junggar basin locates. (B) The tectonic map showing the**
147 **location of the Mahu Sag and main tectonic units of the Junggar Basin. The red polygon represents the**
148 **study region. (C) Well locations within the study region.**

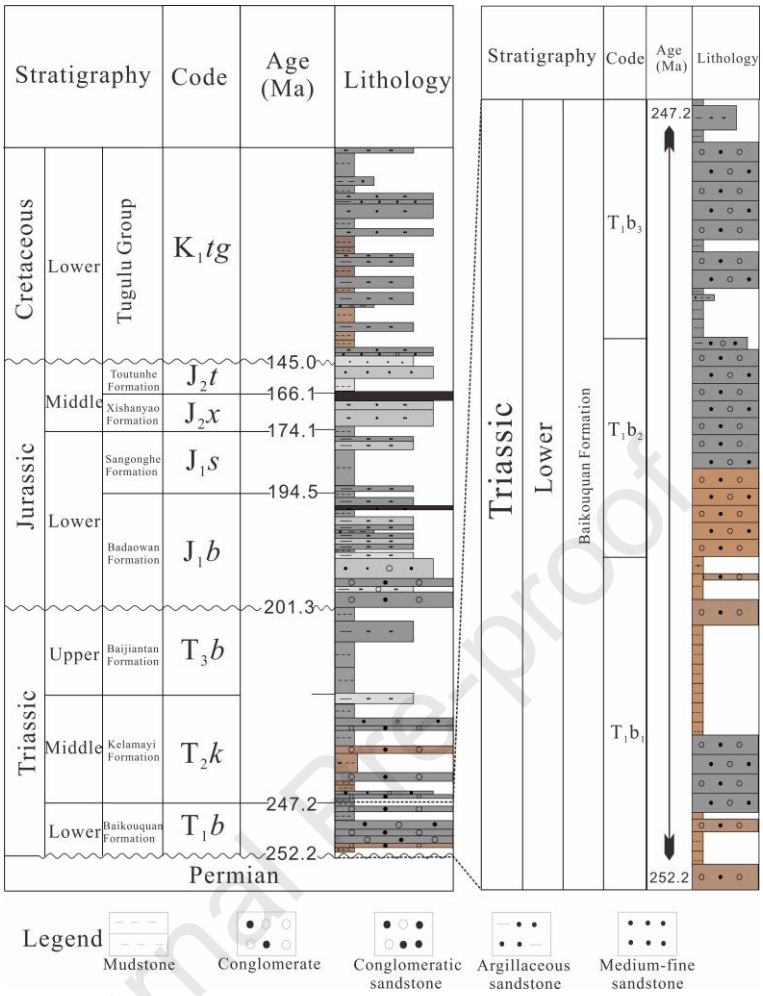

Fig. 2. Synthetical stratigraphic histogram of the strata in the research region. The right-hand side displays a high-resolution sequence of the BF (modified from Xinjiang Oilfield).

3. Materials and Methodology

3.1 Materials

To date, 38 wells have been drilled in the BF, of which 34 are vertical and 4 are horizontal. The wells are sparsely spaced at three wells per square kilometer or one well every 800–1200 m. This study is based on 132 conglomerate samples from the fan delta deposits from 13 boreholes of the BF in different locations at burial depths of 2500–3700 m. 351 thin slice specimens, permeability, and porosity test outcomes of 132 specimens, 306 SEM data, 87 mineral XRD data, grading data, 112 mercury intrusion capillary pressure (MICP) data, along with oil saturation, formation pressure, and well-logging data of the BF in the research area

were acquired from the Research Institute of Petroleum Exploration & Development of the Xinjiang Oilfield Company, PetroChina.

3.2 Optical microscopy analysis

An overall 120 thin slices were injected with blue epoxy for identification of detrital compositions, mineral assemblages, visual pore types, and diagenetic processes by employing a Zeiss microscope. In addition, 64 were also impregnated partly with Red S and K-ferricyanide for carbonate cement investigation. Granule size was obtained via averaging the measurements of the long axes of granules in every thin slice.

3.3 Scanning electron microscopy (SEM)

Posterior to the detailed thin-slice petrographical analyses, 58 typical gold-coated conglomerate samples were selected and imaged to perform microstructural and mineralogic research via a field emission SEM under a JSM-5500 LV SEM with an electron probe microanalyzer (EPMA). The occurrences of cement, 3D minerals, pore geometries, and associations between them can be observed by sending focused beams of electrons and detecting secondary or backscattered electronic signals.

3.4 Cores, and wireline data analysis

Core samples could provide the most direct evidence for lithology and sedimentary microfacies identification. To determine the categorization and spatial distribution of lithofacies and sedimentary microfacies, an overall 253.3 m of cores from 13 wells were detailedly and thoroughly described to examine the rock types, granule size distribution, and sedimentary structures. Moreover, the conventional logs sensitive to lithology include gamma ray (GR) and deep lateral resistivity (RD), which were well-calibrated by cores in this research for detailed lithofacies and sedimentary analysis, enabling the prediction of high-quality reservoirs in the BF.

3.5 Mercury intrusion capillary pressure (MICP) and petrophysical properties

Porosity and permeability measuring was completed on the 132 conglomerate specimens to rank reservoir property of diverse lithofacies and evaluate the impacts of sedimentary microfacies and later diagenetic process on reservoir quality by employing a 3020-62 helium porosity analyzing apparatus and GDS-9F gas permeability analyzing apparatus under ambient temperature and humidity. These samples were measured on plug samples of 2.5 cm diameter. Samples were then washed using distilled water in an ultrasonic cleaner for 5 min and dried at 44 °C for 25 h. Subsequently, 112 specimens that covered the range of permeability and porosity values were chosen to determine the pore-throat distributions using mercury injection (MI) analyses with a 9505 MI analyzing apparatus under 22°C and 60% humidity using the national standard SY/T 5346–2005.

3.6 Fluid inclusion analysis

Thick double-polished thin slices were produced from 67 core specimens from 6 wells for fluid inclusion petrographical analysis, fluorescence color identification, and homogenization temperature (Th) measuring. A Leica polarised light fluorescent microscopic instrument was utilized for fluid inclusion petrographical analysis. Simultaneously, the homogenous inclusion temperature of 32 specimens from 4 wells was measured equipped with a Linkam THMSG600 heating–cooling stage. Fluid inclusions were primarily obtained appearing predominantly in intergranular pores, feldspar dissolution pores, fractures, and quartz from conglomerates of the BF for Th measuring. The equipment could record phase transitions ranging from -180°C to 500°C. The aqueous fluid inclusions were cooled to the lowest temperature, and the phase variations were studied with a slow increase in temperature. The ice-melting temperature was documented under a heating velocity of 0.1°C/min.

3.7 X-ray diffraction (XRD)

To further quantitatively identify mineral constituents in the BF, a total of 87 conglomerate specimens from different locations were produced for whole-rock (bulk) and clay fraction (<2 mm) mineralogical XRD analyses via a Rigaku D/MAX2500 V/PC powder diffractometer. Clay fraction specimens were subjected to XRD analyses after air desiccation, glycolated, and afterward heated to 500°C.

4. Results

4.1 Reservoir features

4.1.1 Petrological analysis

The fan delta reservoirs are mainly fine- to medium-grained (with grain sizes between 2 mm and 16 mm) conglomerates. Detrital quartz takes up 7.3%–30% (mean 12.8%) and predominantly comprises euhedral monocrystalline quartz with poor to moderate sorting. The detrital feldspar content is no more than 10%, with a mean of 4.5%, amongst which the relative amount of plagioclase and K-feldspar is 73% and 27%, respectively (Fig. 3). Varying degrees of argillization and sericitization can be observed on the surface of the feldspar. The rock fragment content ranges between 56% and 85%, with a mean of 65.1%, and comprises 45%–58% of volcanic rocks (mostly tuff), and 11%–27% of sedimentary rocks. Rare content of heavy minerals is present in the reservoirs. The clay amount accounts for 0.5%–40%, with a mean of 8.5%, and the cement amount is 0.5%–22.5% with a mean of 4.6%. The composition maturity, which is equal to the ratio of quartz amount to feldspar and rock fragment amount, is 0.3–0.6 with a mean of 0.4.

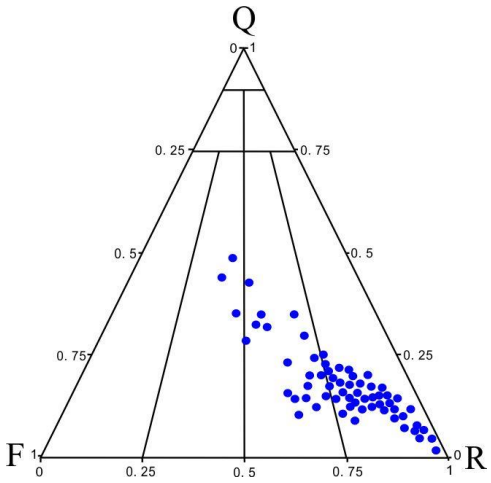

Fig. 3. Ternary QRF diagram presenting the lithofacies feature within the research region (modified from Xinjiang Oilfield).

4.1.2 Physical Properties

The permeability and porosity distribution of the BF in the study area of the Mahu Sag show a wide range of 1.9–16.8% (mean 6.54%) and 0.001 mD to 19.4 mD (average 1.33 mD), respectively (Fig. 4A, B). The percentages of reservoirs with permeability values below 1 mD, 1–10 mD, and over 10 mD were 76.3%, 20.1%, and 3.6%, separately. Approximately 50% of the conglomerate reservoirs belong to low porosity and ultra-low permeability reservoirs. Low permeability (<1 mD) reservoirs with middle-high porosity (>4%) occupy 68% of the total reservoirs (Fig. 4C). There is a wide variation of permeability and porosity within different lithofacies (Fig. 4C). Gravelly sandstone, fine-medium sandstone, and fine-grained conglomerate have good petrophysical properties while medium grained conglomerate possesses lower porosity (Fig. 4C).

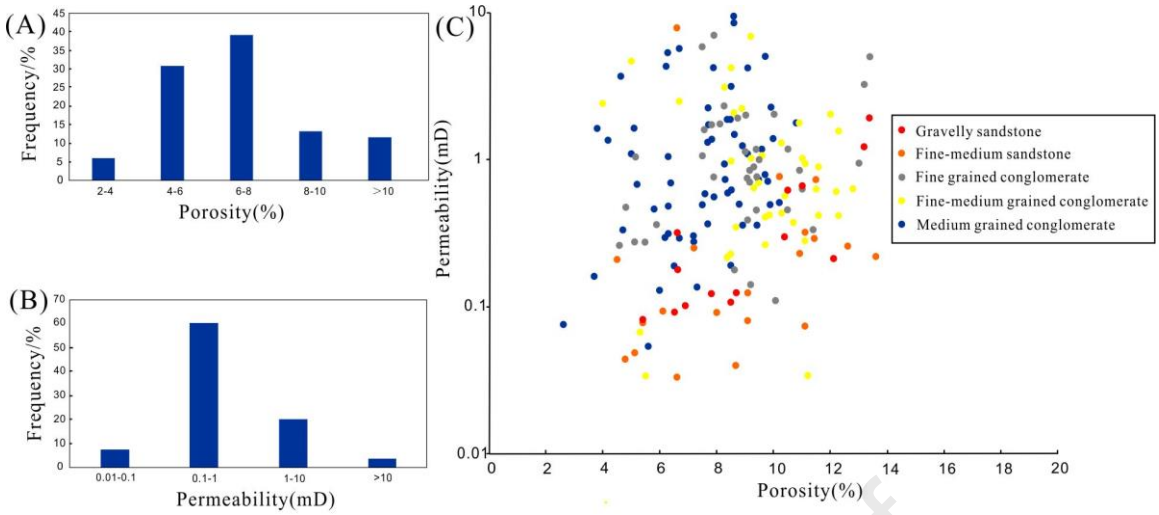

Fig. 4. Porosity and permeability distribution of the fan delta reservoirs in the BF of the Mahu sag. (A) Porosity distributional status histogram. (B) permeability distributional status histogram. (C) Binary diagram of porosity vs permeability.

4.1.3 Pore Types and Pore-Throat Features

Reservoirs with varying permeability are characterized by diverse pore types and distinct pore throat distributions (Fig. 5). The reservoirs with permeability below 1 mD are predominated by porosity ranging from 5%–15% (Fig. 5A). In those reservoir samples, the pores are predominantly micropores in detrital grains or substrate with pore-throat radii (PTR) varying between 0.01 and 1 μm (Fig. 5D, G), and the seepage capacity is under the control of PTR $\leqslant$ 0.1 μm (Fig. 5G). These reservoirs represent the worst petrophysical properties, holding the smallest PTR (average, 0.64 μm), the highest sorting coefficient (2.23–2.83; mean, 2.67), as well as the lowest maximal mercury saturation (Fig. 5H). The reservoirs possessing permeability varying between 1 and 10 mD are primarily composed of 15%–20% porosity (Fig. 5B). Among those reservoirs, the pore types are predominantly secondary pores generated by dissolution of feldspar or rock fragments (Fig. 5E). The PTR range between 0.15 and 9 μm (Fig. 5E, G), and the permeability is governed by PTR between 1 and 4 μm (Fig. 5G, H). The reservoirs with permeability above 10 mD generally have a porosity over 20% (Fig. 5C), among which the pores involve residual intergranular pores and secondary dissolution pores (Fig. 5F), representing the best petrophysical properties, with a sizeable PTR, the smallest sorting coefficient, the highest sorting degree, and the highest maximal mercury saturation (Fig. 5H).

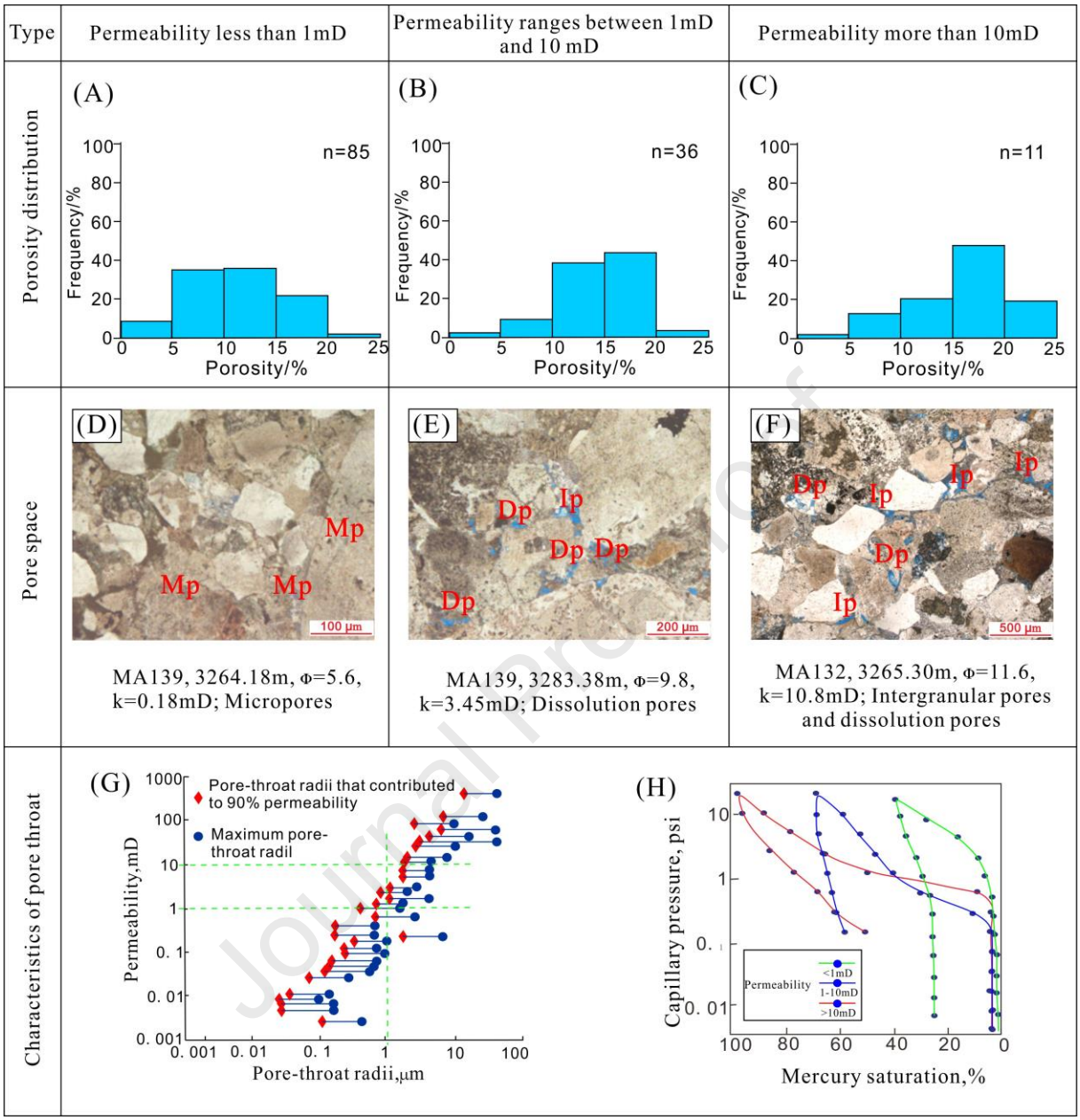

Fig. 5. Features of pores and pore throats of the fan delta conglomerates in the BF of the Mahu sag. (A) Porosity distributional status in reservoirs with permeability below 1 mD. (B) Porosity distributional status in reservoirs with permeability between 1 and 10 mD. (C) Porosity distributional status in reservoirs with permeability above 10 mD. (D) Image of a thin slice presenting pore features in reservoirs with permeability below 1 mD (plane-polarised light). (E) Image of a thin slice presenting pore features in reservoirs with permeability between 1 and 10 mD (plane-polarised light). (F) Image of a thin slice presenting pore features in reservoirs with permeability above 10 mD (plane-polarised light). (G) Binary diagram of PTR vs permeability. (H) Capillary pressure curves with different permeability. Ip = intergranular pore; Mp = micropore; Dp = dissolution pore.

4.2 Reservoir elements of the fan delta deposits

Both gravity flow and tractive flow are in charge of the fan delta deposits. Resultantly, a total of 8 kinds of sedimentary microfacies were encountered during the procedure of detailed core observation, including debris-flow sediments, braided channel filling, and subaqueous distributary channels.

4.2.1 Fan-delta plain

The fan delta plain shares a lot of similarities with the root fan and inner-middle fan of the alluvial fan, wherein coarse-grained lithofacies formed under an aquatic oxidation environment are recorded (Xian et al., 2018). The sediments were generally brown, brownish-red conglomerate. Debris flow, braided river channel, and overflow can be observed in the fan delta plain, which is dominated by the former two microfacies.

4.2.1.1 Debris flow

Debris flow sediments constitute the principal part of the fan delta plain, which is a hybrid accumulation spreading in sheet shape located at the proximal fan delta above the lake level. The lithofacies mainly consisted of brownish red thick medium-grained conglomerate. Matrix-supported structure and thick-layered massive bedding characterize the sedimentary characteristics (Fig. 6A). The gravel sizes generally ranged from 0.6 to 40 mm, with a maximum particle size of up to 100 mm. Its probability curve (PC) of granule size displayed the characteristic of a one-stage style, with an average and median size of ‑ 0.72 φ and ‑ 0.86 φ (φ= ‑ $\log_2 d$, d denotes particulate diameter, mm), respectively (Fig. 7). The gravels were suspended in the sandy or muddy matrix locally and displayed disorderly, without any directionality and imbrication. High RD and GR values showing a thick box shape were observed for the conventional logging response. Sorting was medium to poor, and roundness was subangular to angular. The DP of the MI was 0.75 MPa, with a mean PTR of 0.005 mm, and mercury-ejection efficiency of 24.38% (Fig. 7).

4.2.1.2 Braided river channel

The braided river predominantly comprised brown medium to fine-grained conglomerate, and pebbly sandstone. The PC of the granule size displayed a two-stage style, with a mean particulate size of ‐ 1.52 φ and a median size of ‐ 2.05 φ. The detrital grain exhibited medium to poor sorting characteristics, and the roundness was mainly marked by subangular and subrounded shapes. Imbricate orientation of gravels, and low-angle cross-bedding (Fig. 6B, C) can be observed in the middle and lower part of the channel. Additionally, the sand conglomerate contains erosional surfaces, indicating the recurrent scouring and filling processes of floods. The RD had an overall serrated-box shape, and medium amplitude features. The MI curve suggested a medium pore and fine throat distribution. The DP was 0.26 MPa, and the mean PTR can reach 0.38 mm. Moreover, the efficiency of mercury withdrawal was comparatively satisfactory at 28.56% (Fig. 7).

4.2.1.3 Overflow

The overflow sediments are generated by the depositional process of overflowing water from the sides of braided river channels. The lithology consisted of brown mudstone and siltstone (Fig. 6D). Due to the incision and erosion of channels, the thickness of a single layer is mostly below 0.3 m and is featured by mass bedding. The PC of the granule size displayed a non-typical two-stage style, with an average size of 4.13 φ, and a median size of 3.25 φ The RD curve exhibited serrated-box shapes with a low amplitude. . The mercury injection curve indicated that the mercury withdrawal efficiency was 34.13%, suggesting a micro-pore and fine throat (Fig. 7).

4.2.2 Fan-delta front

Fan delta front and pre-fan delta constitute the underwater part of the fan delta. The lithofacies were generally grayish-green conglomerates packed with sandstone or clay minerals. Sandy debris flow (underwater debris flow), subaqueous distributary channels, interdistributary channels, and mouth bars could be observed via detailed core observation.

4.2.2.1 Sandy debris flow

Sandy debris flow is the underwater extension of debris flow, where similar sedimentary characteristics were observed with debris flow. Its lithology was mainly grayish-green medium-grained conglomerate. The gravels displayed poor sorting, low roundness, and subangular characteristics without directionality and imbrication (Fig. 6E). The PC of the granule size was marked by a low slope and concave shape. The grain size ranged from − 5 φ to 5 φ, with an average size of − 3.19 φ and a median size of − 3.43 φ. The RD curve showed a thick box shape with moderate amplitude. The MI curve suggested that the mean PTR was 0.13 mm, with DP of 0.56 MPa, and a mercury withdrawal efficiency of 17.28% (Fig. 7).

4.2.2.2 Subaqueous distributary channels

The braided river channels progressively transform into subaqueous distributary channels as the hydrodynamics weaken towards the lake basin. The lithology primarily comprised grayish-green fine-grained conglomerate and pebbly sandstone. The gravels showed poorly to moderately sorting and psephicity was commonly sub-rounded to sub-angular. The PC of the granule size showed a typical two-stage style, with a mean particulate size of − 1.23 φ, and a median particle size of − 1.68 φ. Additionally, oil spots were encountered during the procedure of core sample studies (Fig. 6F). In contrast to matrix-supported conglomerates, the clast-supported conglomerate intervals exhibited higher resistivity and lower density values. Low angle cross-bedding, and parallel bedding were recorded in the middle-lower part of the channel. The RD curve was primarily serrated-bell shape with high amplitude, forming positive rhythm sequences vertically. The mercury injection curve showed a DP of 0.53 MPa, a maximal connected PTR of 1.26 mm, and a mercury withdrawal efficiency of 51.86% (Fig. 7).

4.2.2.3 Mouth bars

The mouth bar in the fan delta front is an extension of the subaqueous distributary channel toward the basin. The lithology predominantly consisted of medium-coarse sandstone and pebbly sandstone with cross-bedding and tabular bedding containing low clay amounts,

forming a reverse graded sequence (Fig. 6G). The detrital particle displayed well-sorted, well-rounded characteristics. The RD curve exhibited a serrated-funnel shape with medium amplitude. The PC of the granule size showed a representative three-stage style with a high slope. The MI curve suggested that the DP was 0.52 MPa, accompanied by a mean PTR of 0.25 mm, and a mercury withdrawal efficiency of 24.29% (Fig. 7).

4.2.2.4 Interdistributary channels

Fine-grained sediments deposited between subaqueous distributary channels characterized the interdistributary channels, which predominantly consisted of gray mudstone (Fig. 6H). The PC of the granule size was a representative one-stage style reflecting the suspension component, and the particle size had relatively good sorting with a sorting coefficient of 2.65. The average grain size and median grain size were 3.86 φ, and 3.65 φ, respectively. The RD curve displayed a serrated-finger shape with high amplitude. The mercury injection curve indicated a DP of 2.16 MPa, and a mercury withdrawal efficiency of 36.42% (Fig. 7).

4.2.3 Pre-fan delta

The pre-fan delta was predominantly composed of dark gray horizontal bedding mudstone (Fig. 6I). The sorting of the siltstone is good to excellent with a sorting coefficient of 1.21, indicating a steady hydrodynamical environment. The PC of the granule size displayed a representative two-stage style, of which the jumping component showed a comparatively high slope. The RD curve exhibited a serrated-finger shape with moderate amplitude. The MI curve indicated that the mean PTR was 0.31 mm, accompanied with a high DP of 1.17 Mpa, and a mercury withdrawal efficiency of 33.29% (Fig. 7).

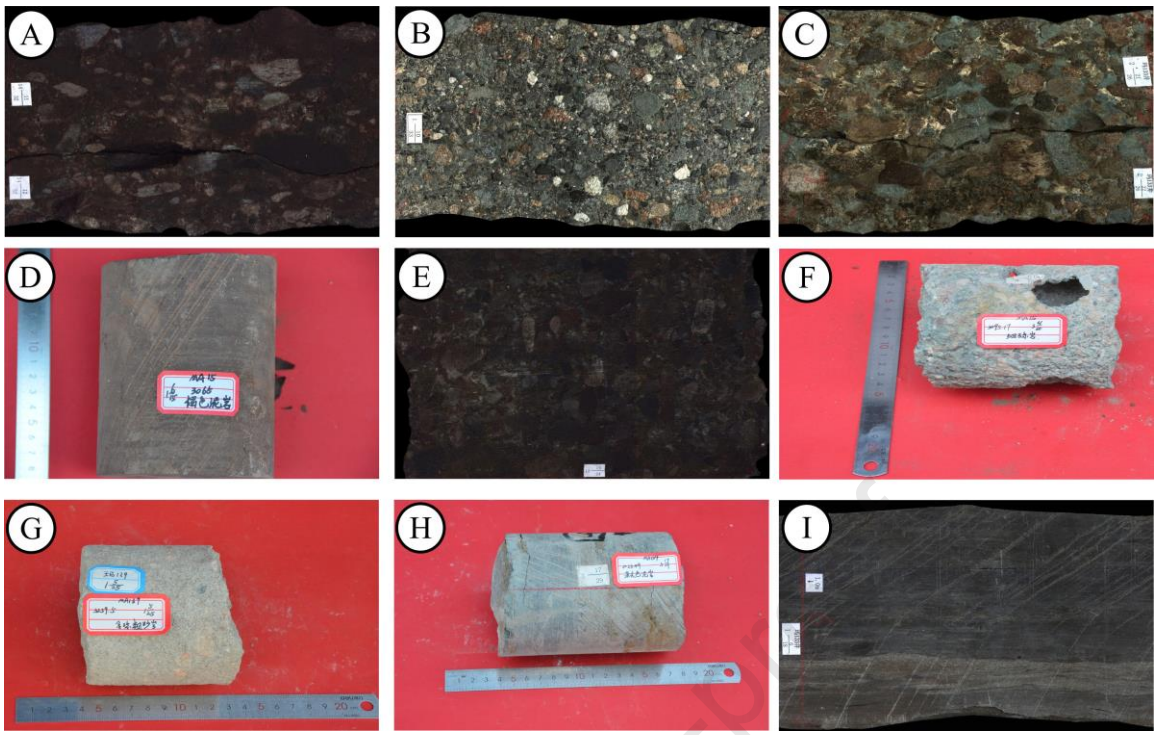

Fig. 6. Characteristics of conglomerate reservoir cores: (A) Matrix-supported medium-grained conglomerates, with grain size larger than 8 mm, massive structure and bedding fracture were encountered, well MA154, 3056.91 m. (B) Clast-supported medium-grained conglomerate, imbricate orientation of gravel, well XIA89, 2231.15 m. (C) Clast-supported coarse-grained conglomerate, with grain size finer than 12 mm, moderate sorted, well MA133, 3302.66 m. (D) Brown mudstone, represents overflow fine-grained fillings, well MA15, 3065.00 m. (E) Matrix-supported conglomerate, with grain size larger than 8 mm, poor sorting, and low roundness, well MA154, 3050.32 m. (F) Clast-supported fine-grained conglomerate, with grain size finer than 8 mm, moderate sorted, well MA15, 3095.17 m. (G) Conglomeratic coarse sandstone, with approximately 7% contents of conglomerates that can be observed, well sorted and rounded, well MA139, 3259.50 m. (H) Gray mudstone, with no obvious development of sedimentary structure, well MA154, 3023.49 m. (I) Dark gray horizontal bedding mudstone, well MA133, 3137.58 m.

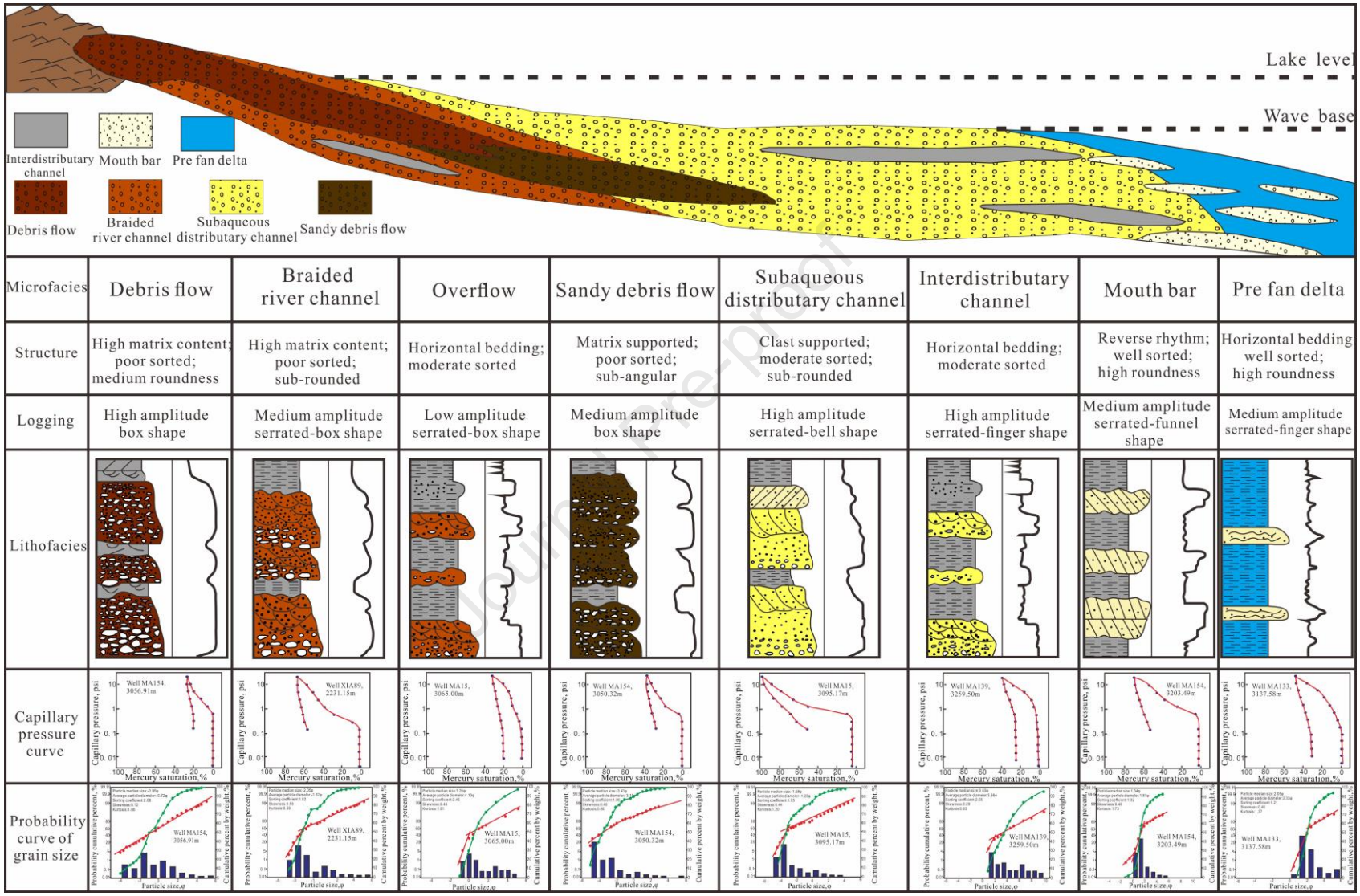

Fig. 7. Sedimentary characteristics of the fan delta deposits in the study area. The scale of the lithofacies is 1:50.

4.3 Diagenesis

4.3.1 Diagenetic Mineralogy

4.3.1.1 Quartz Cement

Siliceous precipitation occurs in the eodiagenesis once the amount of silicon ions in the interstitial water surpasses the mean content. There exist two forms of authigenic quartz in the BF of the fan delta reservoirs, including syntaxial quartz overgrowths around the detrital monocrystal quartz grains and authigenic quartz displaying a euhedral microcrystalline form (Fig. 8A-I). Two phases of syntaxial quartz overgrowths were recorded via thin-section photomicrographs, with a maximum thickness of 25 mm (Fig. 8A-C). The overgrowth rim, which predominantly consisted of either clay minerals or fluid inclusions, was clear (Figure 8A-C). Another type of authigenic quartz appeared as a euhedral prismatic shape filling the pores (Fig. 8D-I), of which the long axis was parallel to detrital particulates, and the margin was covered by authigenic clay minerals like kaolinite, illite-smectite mixed-layer, and chlorite (Fig. 8 D-I). In general, euhedral microcrystalline authigenic quartz predominated because there is not enough substrate available for the homogeneous nucleation of syntaxial quartz overgrowths since the high content of plastic rock debris is believed to have strengthened the compaction degree. The content of quartz cement is less than 2.6% with a mean of 0.7%, increasing slightly as burial depth deepens.

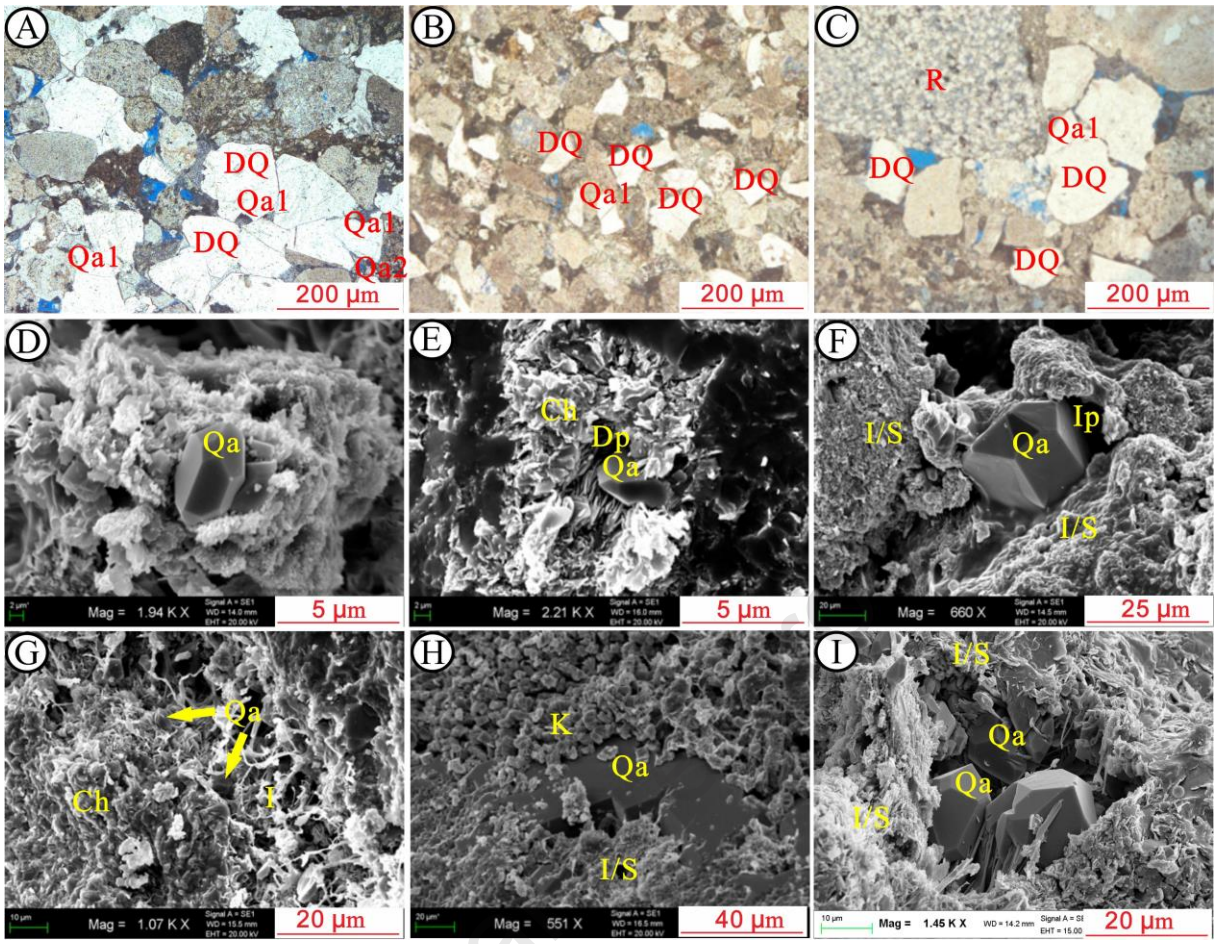

Fig. 8. Characteristics of quartz cement in the fan delta reservoir in the BF of the Mahu sag. (A) Image of a thin slice presenting two phases of quartz overgrowths (plane-polarised light), well XIA89, 2477.27 m. (B) Image of a thin slice presenting quartz overgrowths (plane-polarised light), well MA137, 3251.27 m. (C) Image of a thin slice presenting quartz overgrowths (plane-polarised light), well MA154, 3027.85 m. (D) SEM photomicrograph presenting euhedral Qa, well MA131, 3188.17 m. (E) SEM photomicrograph presenting euhedral Qa and Ch filled the dissolution pore, well MA13, 3109.03 m. (F) SEM photomicrograph presenting euhedral Qa and I/S filled the intergranular pore, well MA13, 3107.29 m. (G) SEM photomicrograph presenting euhedral Qa and I filled the intergranular pore, well MA13, 3109.09 m. (H) SEM photomicrograph presenting euhedral Qa accompanied with I/S and K, well MA131, 3190.79 m. (I) SEM photomicrograph presenting euhedral Qa and I/S filled the intergranular pore, well MA16, 3220.19 m. Qa = authigenic quartz; Ch = chlorite; K = kaolinite; I/S= illite and smectite mixed layer; I = illite; Qa1 = first phase of quartz overgrowth; Qa2 = second phase of quartz overgrowth; DQ = detrital quartz; R = rock fragment; Ip = intergranular pore; Dp = dissolution pore.

4.3.1.2 Carbonate Cement

Carbonate cements are the most commonly seen cement in the BF, including calcite, ferroan calcite, and ankerite. According to the XRD data, their mass fraction range between 1% and 11%, with a mean content of 3.47%. Similar to quartz cement, two phases of carbonate cement can be recognized via thin slices and SEM examination. The color of calcite cement varied from red to blue in the dyed thin slices, where the calcite was always red, the ferroan calcite cement was deep red, and ankerite cement exhibited blue tint (Fig. 9A-C) (Gier et al., 2008). Calcite produced in diverse diagenetic phases displayed distinct crystallinity and crystal size. The crystals formed in the eodiagenesis were smaller because of poor crystallinity, whereas those produced in the mesodiagenesis were larger and filled intergranular pores and dissolution pores in either poikilotopic blocks or pore-filling style (Fig. 9A-E), resulting in the sharp exacerbation of reservoir petrophysical properties. Furthermore, the early carbonate cement had undergone later dissolution, forming intracrystalline dissolved pores (Fig. 9F, G) thereby enhancing the reservoir petrophysical properties. In the meanwhile, it also provided calcium ions for late carbonate cementation. It is widely believed that the content of carbonate cement elevates as the distance between the mudstone and sandstone interface reduces because the source of carbonate cement is closely tied to mudstone (Fig. 9H, I) (Warnecke et al., 2019). For instance, the calcium ions released during the maturation of organic matter in mudstone can provide material sources for carbonate cementation (Feng et al., 2019; Xu et al., 2019).

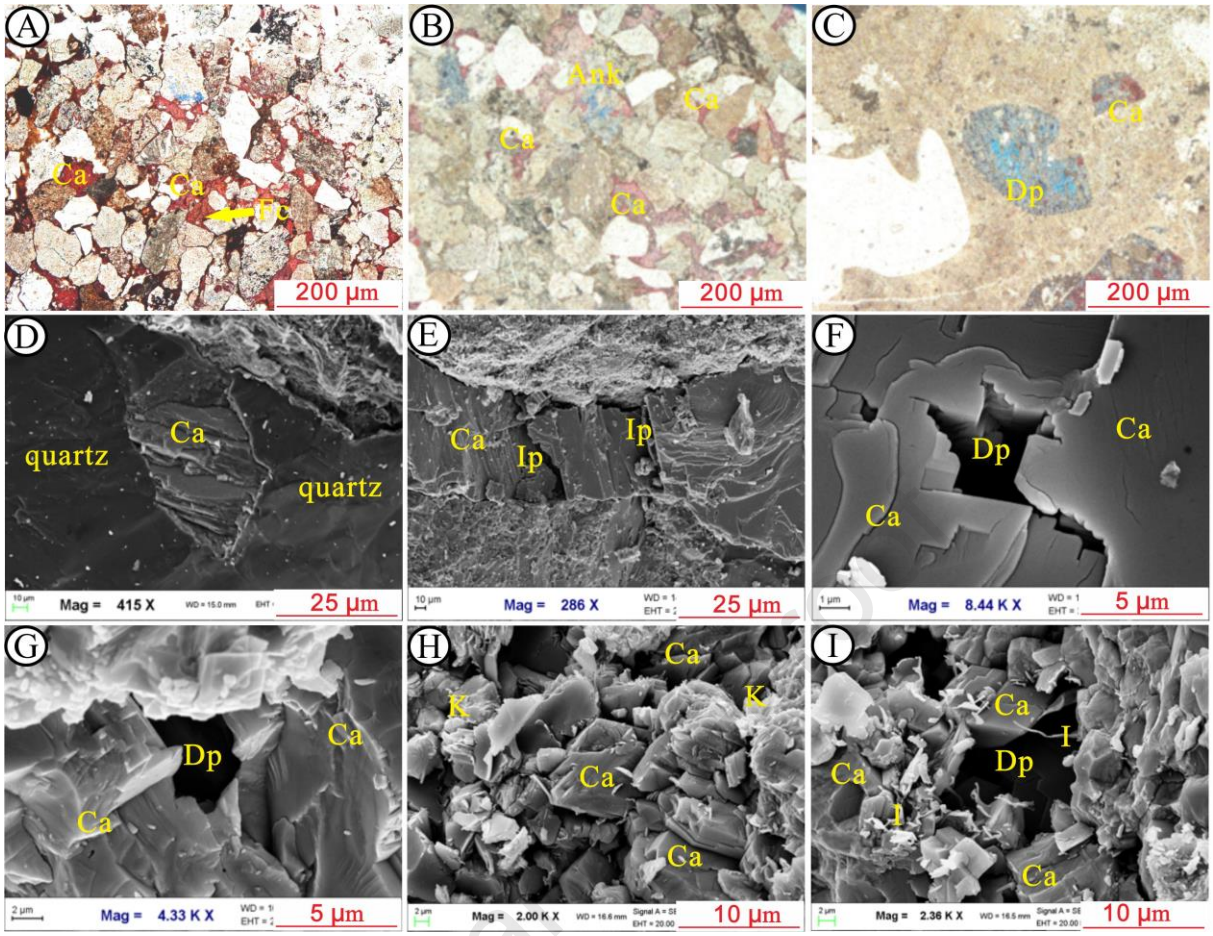

Fig. 9. Characteristics of carbonate cement in the fan delta reservoir in the BF of the Mahu sag. (A) Image of a thin slice presenting Ca with ferroan calcite (plane-polarised light), well MA154, 3027.85 m. (B) Image of a thin slice presenting Ca with ankerite (plane-polarised light), well XIA723, 2699.72 m. (C) Image of a thin slice presenting dissolution pore filled by calcite (plane-polarised light), well MA132, 3268.78 m. (D) SEM image presenting calcite filled the quartz, well MA139, 3315.24 m. (E) SEM image presenting calcite filled the intergranular pore, well MA154, 3005.43 m. (F) SEM image presenting intracrystalline dissolved pore, well MA154, 3030.78 m. (G) SEM image presenting intracrystalline dissolved pore, well MA154, 3044.96 m. (H) SEM image presenting Ca and K filled the intergranular pore, well MA134, 3217.69 m. (I) SEM image presenting Ca and I filled the dissolution pore, well MA134, 3217.79 m. Ca = calcite; Fc = ferroan calcite; Ank = ankerite; K = kaolinite; I = illite; Ip = intergranular pore; Dp = dissolution pore.

4.3.1.3 Dissolution of unstable components

Dissolution is of great significance for enhancing reservoir petrophysical attributes throughout the entire diagenetic process (Zhu et al., 2010). The findings from thin slices and SEM showed that the dissolution of feldspar and rock debris was intimately associated with kaolinite and authigenic quartz (Fig. 10A-D), indicating an acid diagenetic environment. Feldspar preferentially dissolved along the cleavages, and certain feldspars were nearly completely dissolved, yielding an extra induced porosity (Fig. 10E, F). As the diagenetic environment turned into to an alkaline environment, partial secondary pores generated by feldspar dissolution were observed to be filled by subsequent diagenetic minerals like illite, illite-smectite mixed-layer, and carbonate cement (Fig. 10G–I). The content of these unstable components was between 0.3% and 6.5% with a mean of 2.8%. The dissolution intensity slightly elevated as burial depth deepened.

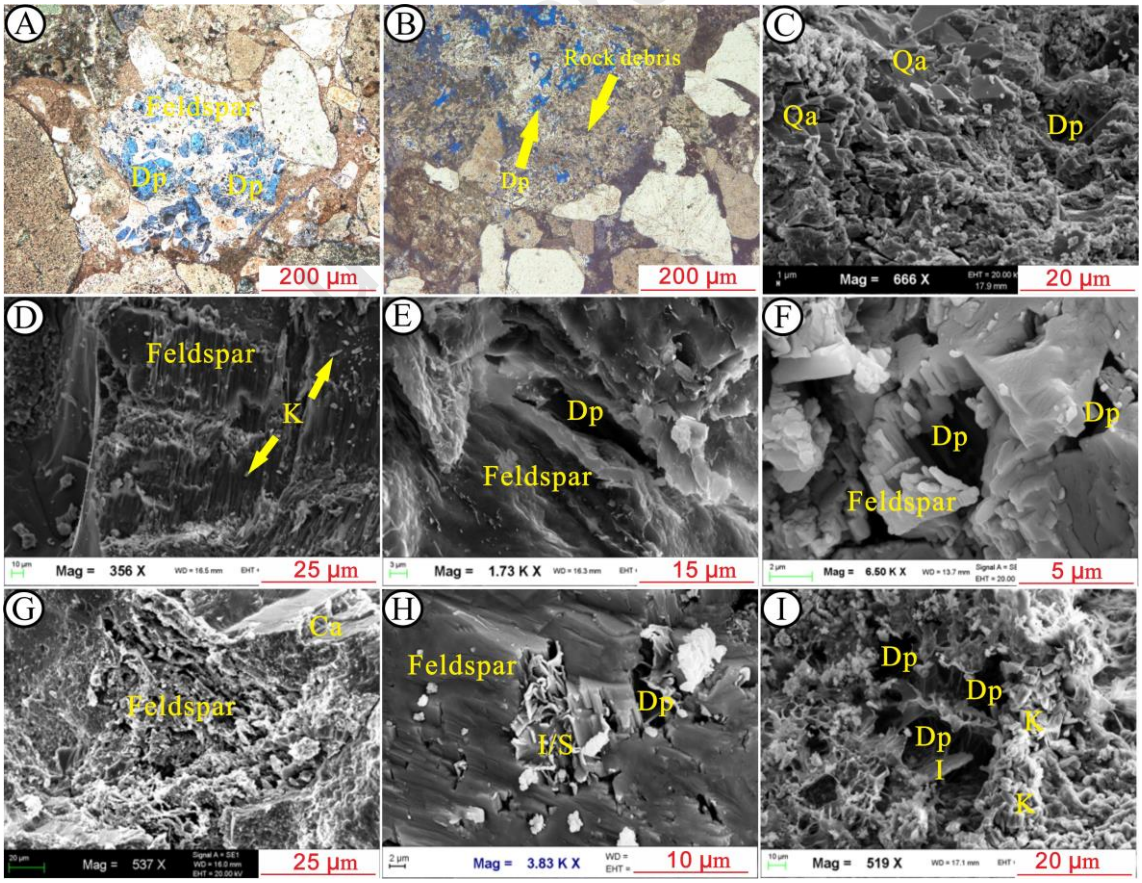

Fig. 10. Features of dissolution of unstable components in the fan delta reservoir in the BF of the Mahu sag. (A) Image of a thin slice presenting the feldspar is almost completely dissolved (plane-polarised light), well MA154, 3051.83 m. (B) Image of a thin slice presenting dissolution of rock debris (plane-polarised light), well MA152, 3096.70 m. (C) SEM image presenting the dissolution

accompanied by Qa, well MA137, 3263.36 m. (D) SEM image presenting the dissolution accompanied by K, well MA139, 3316.24 m. (E) SEM image presenting the intragranular dissolution pore, well MA137, 3264.52 m. (F) SEM image presenting the intragranular dissolution pore, well MA133, 3364.86 m. (G) SEM image presenting the dissolution pore filled by calcite, well MA13, 3107.29 m. (H) SEM image presenting the dissolution pore filled by I/S, well MA132, 3279.28 m. (I) SEM image presenting the dissolution pore filled by I, well MA139, 3270.42 m. Ca = calcite; Qa = authigenic quartz; K = kaolinite; I = illite; I/S= illite and smectite mixed layer; Dp = dissolution pore.

4.3.1.4 Clay Minerals

The research into clay materials is a pivotal part of diagenesis which could help determine and divide diagenetic phases (Jin et al., 2018). The clay fraction (<2 mm) from XRD and SEM image data indicated that kaolinite, illite-smectite mixed-layer, and chlorite dominated the clay minerals. During the eodiagenesis, kaolinite occurred as worm-shaped aggregates in residual intergranular pores and feldspar dissolution pores (Fig. 11A). The euhedral kaolinite had an intimate association with feldspar dissolution and authigenic quartz precipitation (Fig. 11B). Illite-smectite mixed-layer appeared in a honeycomb-like shape in the pore throat (Fig. 11C), severely deteriorating the seepage capacity of the reservoir. The fibrous illite was either coupled with illite-smectite mixed-layer or filled the pores in a bridging style (Fig. 11D-F). Diverse clay minerals are capable of converting into one another. As the diagenetic environment was converted to an alkaline environment, kaolinite turned into chlorite under the existence of iron and magnesium ions (Meng et al., 2020). Chlorite rosettes filled the pores or wrapped the surface of detrital grains (primarily quartz and feldspar) as chlorite coatings (Fig. 11G, H), iron ions of which were mainly acquired from the alteration of volcanic rock debris (Grigsby, 2001). It's broadly believed that such a chlorite membrane prevented the particulates from contacting the interstitial water, which has restrained the overgrowth of quartz (Cao et al., 2018; Griffiths et al., 2021; Li et al., 2021; Molenaar et al., 2021). In addition, the transformation of smectite to euhedral chlorite was also observed (Fig. 11I). The content of clay minerals was 12.6% on average, whereas chlorite and illite-smectite mixed-layer dominated with an average relative content of 32.7%, and 21.3%, respectively. The comparative content of kaolinite reduced at burial depths exceeding 3000 m (Fig. 12). In contrast, the comparative content of illite, chlorite,

and illite-smectite mixed layer showed elevating trends when the burial depth surpassed 3000 m (Fig. 12).

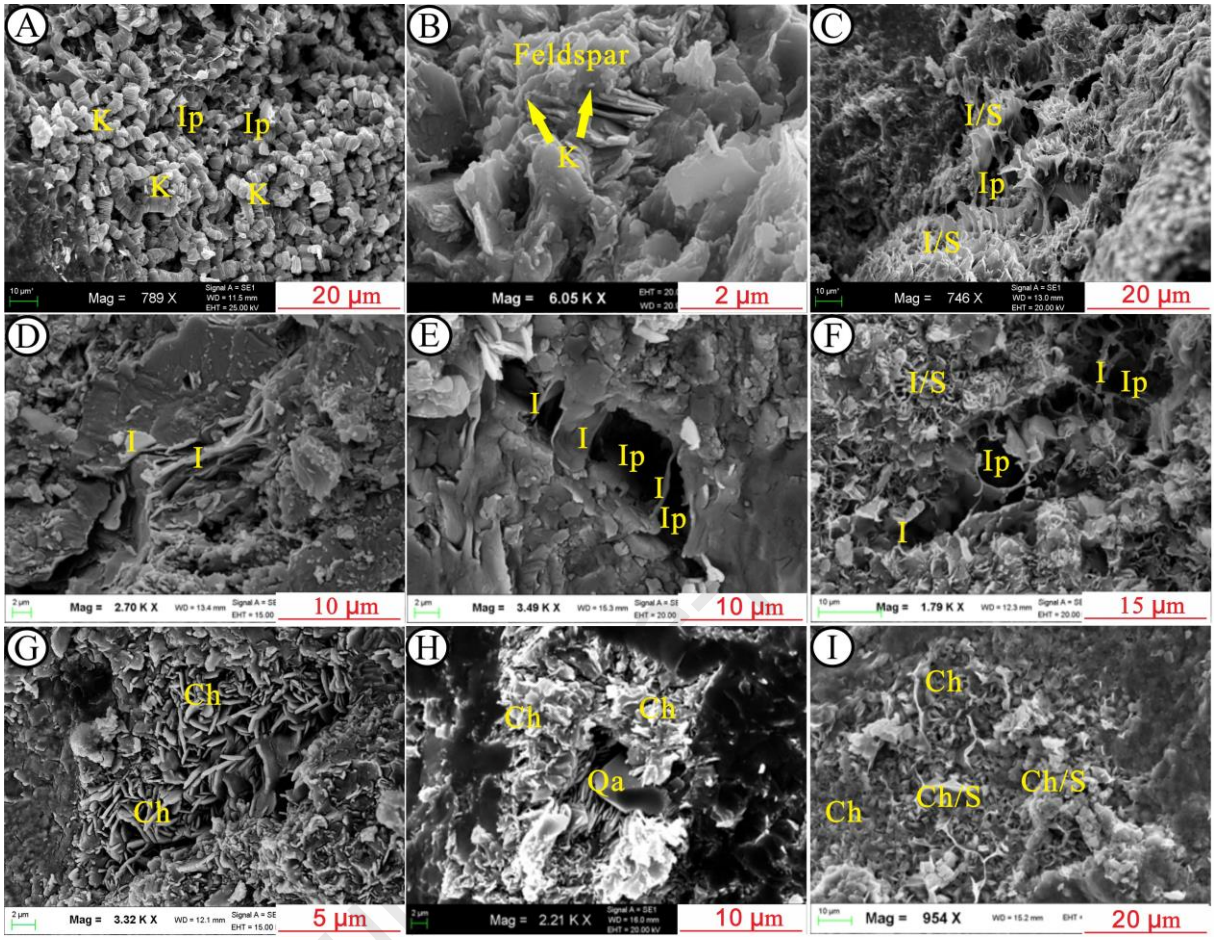

Fig. 11. Characteristics of clay minerals in the fan delta reservoir in the BF of the Mahu sag. (A) SEM image presenting worm-shaped kaolinite filled the Ip, well MA132, 3261.37 m. (B) SEM image presenting K occurred within the dissolution of feldspar, well MA136, 3325.23 m. (C) SEM image presenting the honeycomb-like I/S appeared around the particle surface, well MA131, 3188.89 m. (D) SEM image presenting the curved sheet I appeared around the particle surface, well MA16, 3215.74 m. (E) SEM image presenting the intergranular pore filled by I in a bridging style, well MA134, 3211.95 m. (F) SEM image presenting the intergranular pore filled by I and I/S, well MA133, 3310.72 m. (G) SEM image presenting the Ch wrapped the surface of detrital grains, well MA16, 3213.77 m. (H) SEM image presenting the Ch filled the Ip, well MA13, 3109.03 m. (I) SEM image presenting the Ch and Ch/S appeared around the particle surface, well MA137, 3257.30 m. Qa = authigenic quartz; K = kaolinite; I = illite; I/S= illite and smectite mixed layer; Ch/S= chlorite and smectite mixed layer; Ip = intergranular pore.

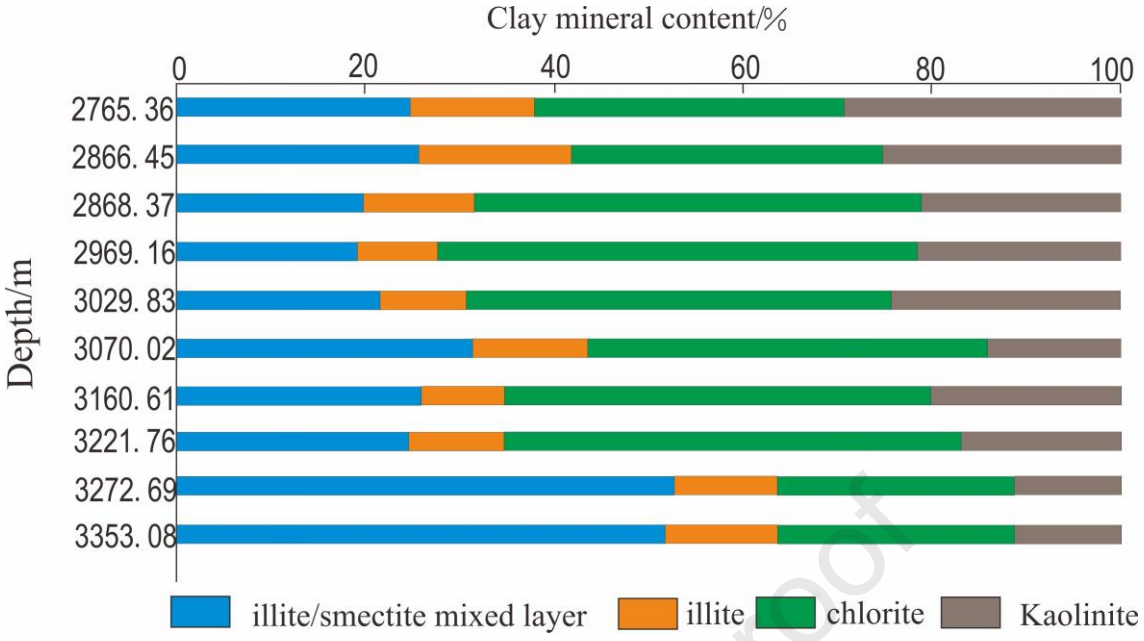

Fig. 12. Content of clay minerals from XRD data in the fan delta reservoir in the BF of the Mahu sag.

4.3.1.5 Other Diagenetic Minerals

Other diagenetic minerals observed via SEM photomicrographs include pyrite, zeolite, apatite, halite, dickite, and zircon (Fig. 13A-L). Pyrite appeared as irregular pore-filling crystals, closely tied to clay minerals like illite-smectite mixed-layer and illite (Fig. 13A, B). Apatite exhibited as endophytic columnar crystals engulfed by feldspar or clay minerals (Fig. 13C-E), and its material source generally originated from basic or alkaline igneous rocks. Zeolite rosettes typically formed in the fissures of volcanic rocks during the mesodiagenesis and filled the pores (Fig. 13F, G), thus deteriorating reservoir petrophysical properties. Dickite has similar composition but a distinct crystal structure to kaolinite, and it showed a tower-like shape filling the intergranular pores (Fig. 13H, I). Halite crystals precipitated around the particle surface (Fig. 13J, K). Zircon was observed to develop around the surface of the detrital grain (Fig. 13L), and it is widely employed in provenance analysis due to its stable chemical properties (Shan et al., 2016). Those diagenetic minerals have a total amount of $<$ 1%.

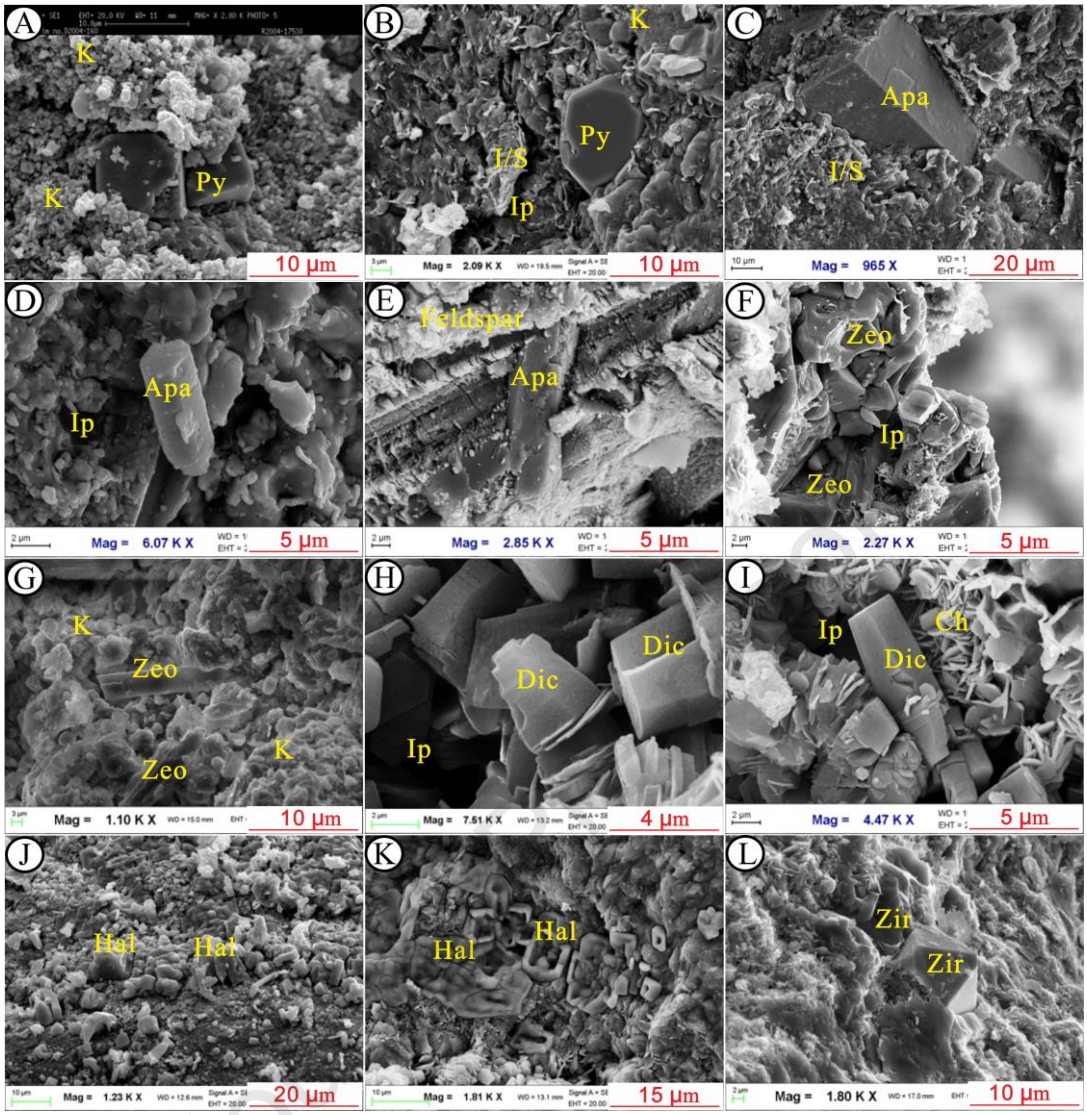

Fig. 13. Features of minor diagenetic minerals in the fan delta reservoir in the BF of the Mahu sag. (A) SEM photomicrograph showing Py crystals filled the Ip, well XIA201, 2732.11 m. (B) SEM photomicrograph showing Py appeared around the particle surface, well MA134, 3217.02 m. (C) SEM photomicrograph showing the endophytic Apa columnar crystals engulfed by I/S, well MA132, 3274.39 m. (D) SEM photomicrograph showing the endophytic Apa columnar crystals, well MA132, 3268.69 m. (E) SEM photomicrograph showing the endophytic Apa columnar crystals engulfed by feldspar, well MA154, 3056.78 m. (F) SEM photomicrograph showing the Zeo crystals filled Ip, well MA132, 3275.62 m. (G) SEM photomicrograph showing the Zeo crystals accompanied with K, well MA137, 3249.59 m. (H) SEM photomicrograph showing the Dic filled the Ip, well MA134, 3171.33 m. (I) SEM photomicrograph showing the Dic filled the Ip, well MA154, 3026.81 m. (J) SEM photomicrograph showing the Hal precipitated around the particle surface, well MA134, 3174.58 m. (K) SEM photomicrograph showing the Hal precipitated around the particle surface, well MA134, 3170.16 m. (L) SEM photomicrograph showing the Zir precipitated around the particle surface, well MA137, 3264.18 m. Py = pyrite; Apa = apatite; Zeo = zeolite; Dic= dickite; Hal= halite; Zir = zircon.

4.3.1.6 Oil Presence

Oil charge is one of the most vital diagenetic events that significantly affect the diagenetic process (Li et al., 2020). Pan et al. (2021) stated that the primary source rocks of the Mahu Sag are the Permian Fengcheng (P_1f) and Wuerhe Formations (P_2w), and two hydrocarbon charging periods occurred in the BF. To sum up, the first phase of hydrocarbon charging emerged in the early Jurassic, causing the trapping of yellow-fluorescence inclusions, which were observed primarily in intergranular pores, fractures, and quartz (Fig. 14A-E). The second phase of hydrocarbon charging emerged in the early–middle Cretaceous, trapping blue-fluorescence hydrocarbon inclusions mainly occurring in feldspar dissolution pores, ferroan calcite, and clay minerals like kaolinite (Fig. 14D-I). The colors of organic materials under an ultraviolet microscope reflect different hydrocarbon maturity: yellow fluorescent results indicate hydrocarbon that is relatively immature, while blue fluorescent results denote hydrocarbon with higher maturity.

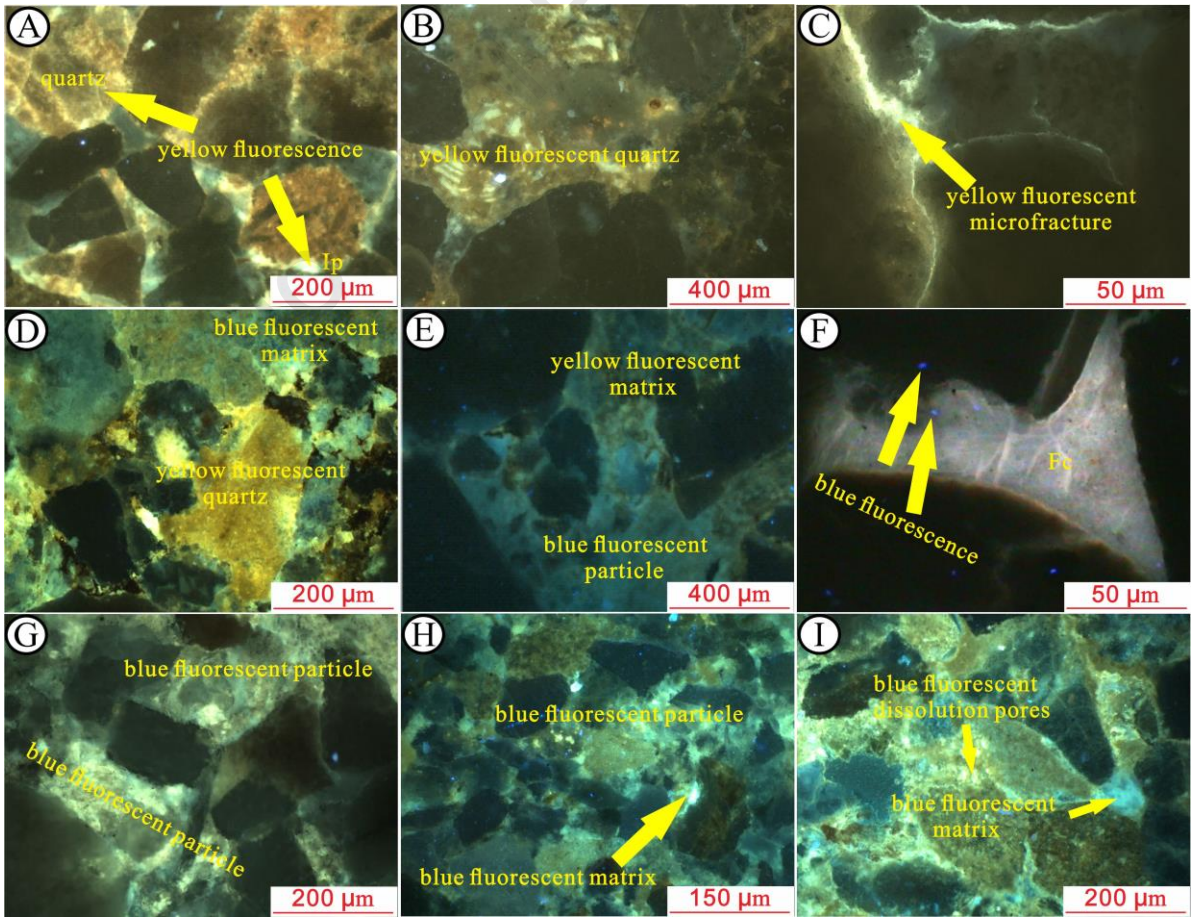

Fig. 14. Fluorescent images presenting the range in colors displayed by the oil inclusions. (A) hydrocarbon with yellow fluorescence preserved in quartz and Ip, well XIA92, 2506.90 m. (B) liquid

hydrocarbons with yellow fluorescence observed in quartz particle, well XIA89, 2447.00 m. (C) hydrocarbon with yellow fluorescence preserved in microfracture, well XIA93, 2703.87 m. (D) yellow-fluorescent hydrocarbon preserved in the detrital grain and blue-fluorescent hydrocarbon filling the matrix, representing two phases of hydrocarbon charging, well MA15, 3069.78 m. (E) little yellow-fluorescent hydrocarbon exhibited in the matrix and blue-fluorescent hydrocarbon preserved in the matrix and detrital grain, representing two phases of hydrocarbon charging, well MA134, 3193.33 m. (F) blue fluorescent hydrocarbon stored in dissolution pores of Fc, well XIA72, 2122.55 m. (G) blue fluorescent hydrocarbon stored in detrital grains and matrix, well MA136, 3323.04 m. (H) blue fluorescent hydrocarbon stored in detrital grains and matrix, well MA17, 3249.33 m. (I) liquidic blue fluorescent hydrocarbon filling the dissolved feldspar pores and matrix, well MA16, 3213.84 m.

4.3.2 Paragenetic Sequence of Diagenetic Events

Chlorite coatings formed in the Early Triassic to Early Jurassic during the eodiagenesis at a formation temperature of 55-70 °C (Fig. 15). The pore-filling chlorite, authigenic kaolinite, and quartz that formed in the secondary dissolution pores all exhibited well-euhedral characteristics. Additionally, the material source of these minerals primarily originated from the dissolution of unstable components like feldspar and tuffaceous rocks (Tang et al., 2021). It can be inferred that the dissolution of unstable components occurred earlier than the precipitation of authigenic kaolinite and quartz cement. Calcite engulfs ferroan calcite and thus postdates ferroan calcite (Fig. 9A). Ankerite fills the pore space between calcite and detrital grain (Fig. 9B). On the foundation of the replacement relation of carbonate cement, the precipitation sequence of carbonate cement is (1) ferroan calcite, (2) calcite, and (3) ankerite. Additionally, the dissolution of calcite was observed under the microscope, indicating that the precipitation of calcite must have predated the dissolution of unstable components.

On the foundation of burial history, and diagenesis, the paragenetic sequence of the conglomerate reservoir in the BF can be summarized in Fig. 15. Compaction continued throughout its entire burial. The reservoir within the target layer has generally experienced alkaline, acid, weak alkaline, acid, and weak acid diagenetic environment (Jin et al., 2017). During the eodiagenesis, the stratum was rapidly subsiding with a formation temperature lower than 65 ℃. The rock was semi-consolidated at the initial period of sedimentation. Meanwhile, the alkaline reduction diagenetic environment contributed to the formation of chlorite coatings and precipitation of analcite. Subsequently, montmorillonite will progressively transform into

611 illite-smectite mixed layer as formation temperature and pressure rise with increasing burial
612 depth. Thereafter, the first phase of hydrocarbon charging emerged in the early Jurassic, where
613 the formation temperature can approach 70℃ and the diagenetic environment turned into an
614 acid environment due to the acidic fluids generated by compression of mudstones. This process
615 also contributed to the later dissolution of unsteady constituents like feldspar and tuffaceous
616 rocks, precipitation of authigenic kaolinite, as well as quartz overgrowth. As the dissolution
617 proceeds, the concentration of organic acid decreases, and the alkaline metal ions produced by
618 rock debris and feldspar entered the pore water, thus providing materials for the precipitation
619 of calcite. Subsequently, the second phase of hydrocarbon charging took place in the early–
620 middle Cretaceous, where blue fluorescence was observed in feldspar-dissolution pores. The
621 diagenetic environment turned into an acid environment again, and the enrichment of calcium
622 ions released by dissolution of unstable components induced the precipitation of late-stage
623 calcites. However, it is noteworthy that not all reservoirs in the BF of the Mahu sag have
624 encountered the whole paragenetic sequence aforesaid. For instance, the clay-rich debris flow
625 deposits may have merely encountered tight compaction and late calcite cementation before
626 becoming tight reservoirs.
627

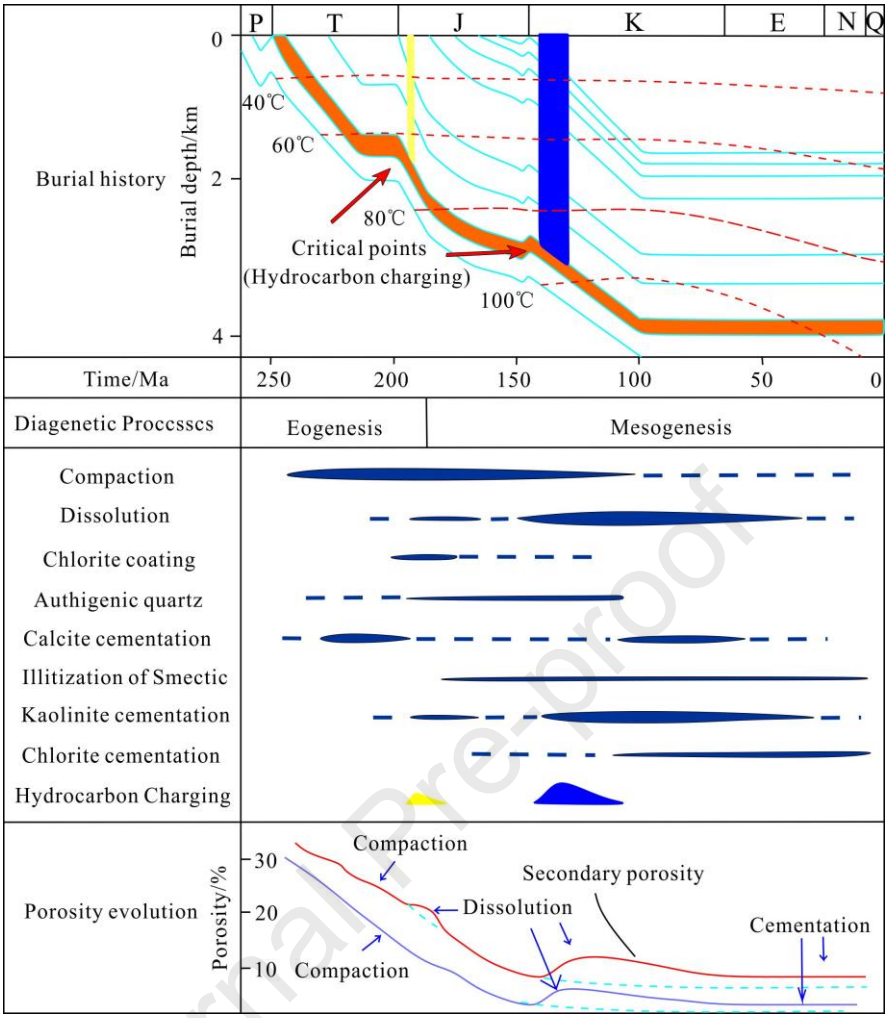

Fig. 15 Integrated diagenetic process on the foundation of the diagenesis aspects, burial and heat history, and its roles in porosity in the sandy conglomerates in the BF of the Mahu sag (modified from Kang, 2019). The red line and blue line denote the main diagenetic event of fine-grained conglomerates and medium-grained conglomerates, respectively.

5. Discussion

5.1 Effect of sedimentary processes on reservoir quality

Sedimentation has a remarkable influence on facies distribution, granule size, and clay amount, causing spatial variations of reservoir quality in the fan delta deposits (Wu et al., 2020). During the deposition of the BF, surrounding mountains like Halaalate on the northwest margin provided a sufficient material source for the deposition of the fan delta system. The palaeogeomorphology in the early Triassic generally governed the flow pattern and the

macrodistribution of sand bodies (Yu et al., 2022). Moreover, the climate also exerted a remarkable impact on the sedimentary filling process of the fan delta complex. Few plants capable of fixing soil in an arid-semiarid climate led to frequent paroxysmal floods and debris flows following the rainy season, thus forming a fan delta complex containing much higher gravity flow deposits in the Mahu Sag (Yao et al., 2017). Resultantly, the fan delta plain is dominated by the offloading of debris flow sediments near provenance. The coarser grain and high clay content fraction at the base of gravity flow will first settle, whereas the finer grains at the top of flows progressively deposit in the fan delta front areas. From proximal to distal fan delta, the spatiotemporal distribution of lithofacies associations was recognized in the BF of the Mahu oilfield (Fig. 7), indicating a progressive conversion from cohesive muddy debris flow into traction current (Fig. 16).

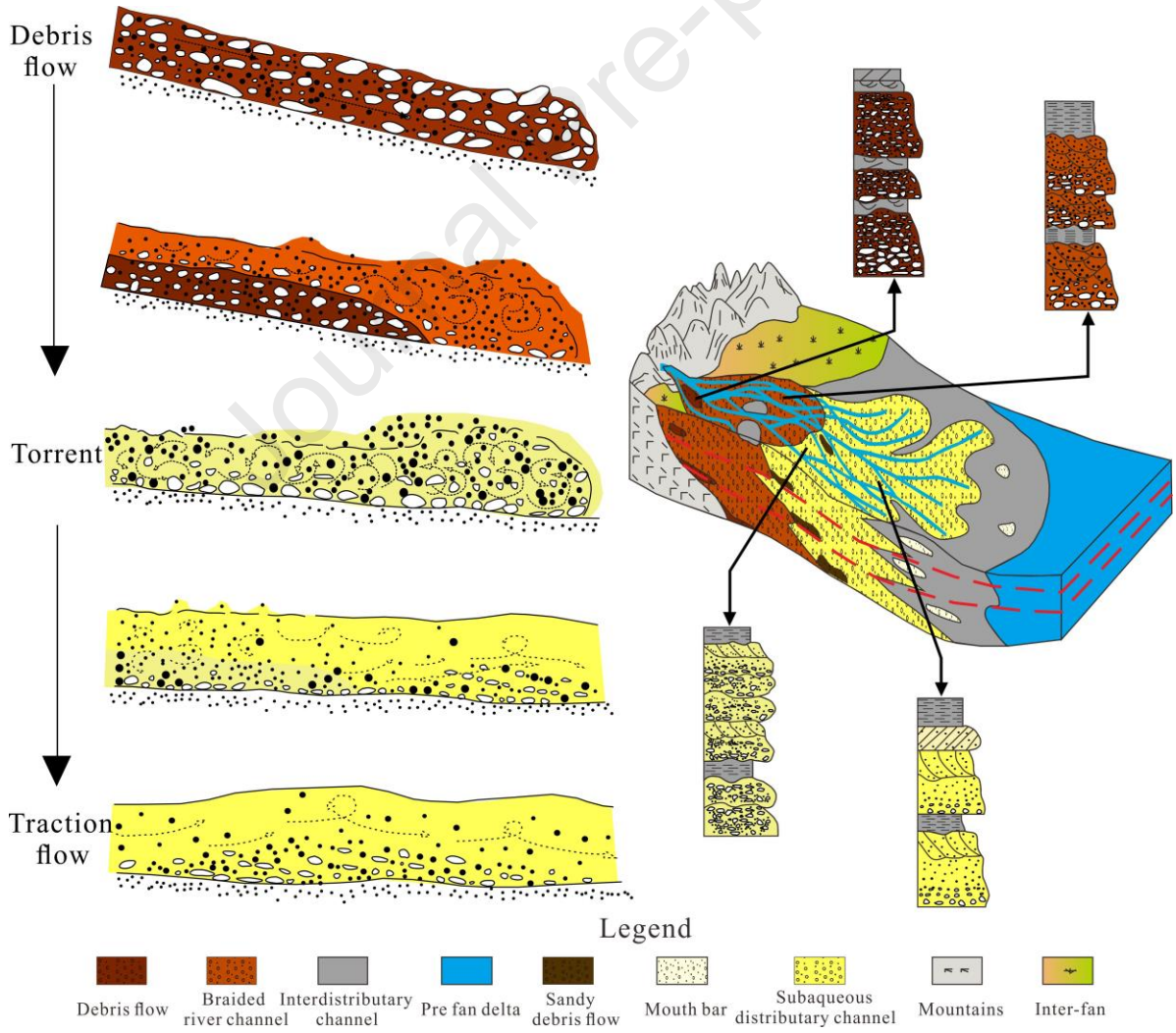

Fig. 16 Illustration of sedimentary process presenting the spatial variations of reservoir quality in the fan delta deposits.

Pivotal sedimentary factors remarkably affecting the reservoir quality involve granule size, sorting, granule morphology, and muddy content in the sandy conglomerates. The relationship between the permeability and porosity in Fig. 4C reveals that reservoir quality is associated with the deposition milieu and the impact of the diagenetic process. We have plotted the sorting coefficient, average grain size, and muddy content versus permeability and porosity, split by microfacies to assess their impacts on reservoir quality (Fig. 17A-F). Subaqueous distributary channel and mouth bar had relatively lower sorting coefficients because their sediments were transported for long distances, thus the particles were well-sorted and the petrophysical properties exhibited higher values (Fig. 17A, B). Another significant determinant in reservoir quality is grain size variation arising from sediment gravity differentiation. Nevertheless, an intricate association exists between the granule size and reservoir quality (Fig. 17C, D). As shown in Fig. 17C, the subaqueous distributary channel and mouth bar had finer grain size and superior porosity. However, the permeability in the near-shore subaqueous distributary channel with coarse grain size showed higher values than those in the far-shore subaqueous distributary channel (Fig. 17D). This is probably attributed to the comparatively high muddy content in the far-shore subaqueous distributary channel (Fig. 17F). Cast thin section observation and petrophysical measurements have demonstrated that the muddy content negatively affects reservoir permeability and porosity (Fig. 17E, F). The porosity drops from 13% to 7% with increasing muddy content from 1% to 7% (Fig. 17E), but there is an abrupt decrease in permeability of more than two orders of magnitude (from 32 to 0.2 mD) (Fig. 17F), that is, the seepage capacity of the reservoir is severely deteriorated by argillaceous matrix residues in the pore throat. Collectively, it is concluded that the sedimentary process influenced the spatiotemporal macrodistribution of reservoir quality within the fan delta complex.

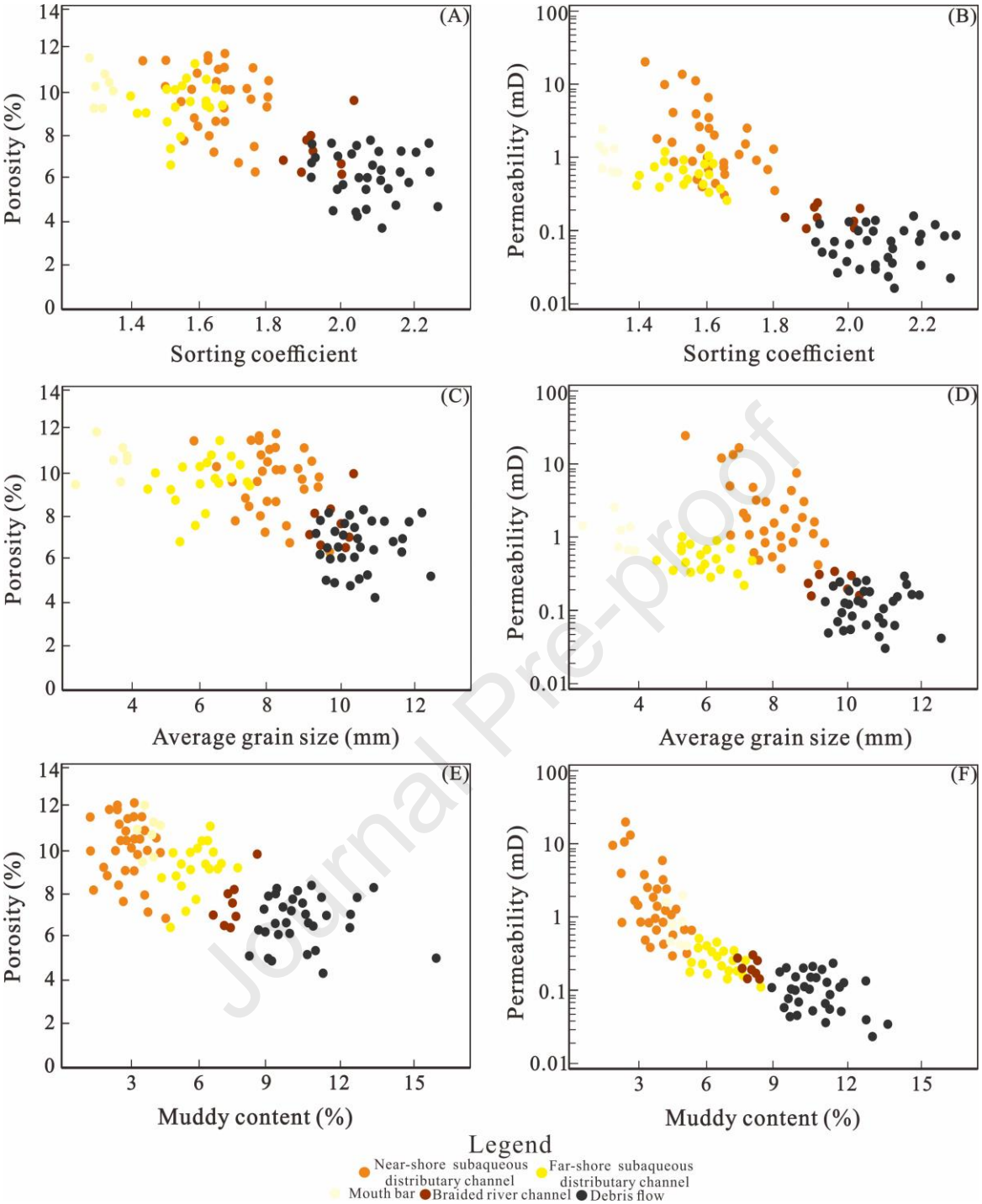

Fig. 17 Crossplot of reservoir attributes split by microfacies. (A) Sorting coefficient vs core porosity; (B) sorting coefficient vs permeability; (C) mean granule size vs core porosity; (D) mean granule size vs permeability; (E) muddy content vs core porosity; (F) muddy content vs permeability.

5.2 Diagenetic Control on Reservoir Quality

5.2.1 Compaction

The lithofacies in the Triassic BF are featured by low structural maturity and high content of argillaceous matrix (especially brown argillaceous sandy conglomerate) (Yu et al., 2022). The content of the argillaceous matrix is one of the key factors affecting compaction and reservoir petrophysical properties. A significant portion of the argillaceous matrix can inhibit the development of carbonate cementation during eodiagenesis. Resultantly, the compaction is more likely to destroy the primary intergranular pores without the supporting framework of early carbonate cement. Furthermore, the relatively strong lubrication of the argillaceous matrix enhances the destructive force of mechanical compaction on reservoir petrophysical properties. These plastic particles tend to be compressed and deformed as burial depth exceeds 3000 m, resulting in a sharp deterioration of the physical properties (Zhang et al., 2018).

Petrological evidence demonstrates that conglomerate compaction in the BF in the research region is stated below (i): particles exhibit plastic distortion (e.g. the rock debris is crooked, deformed) (Fig. 9B), and (ii): particles display point-line and concave-convex contact relationship (Fig. 10B). Thin section observation suggests strong compaction in the study area, causing a sharp decrease in the pore spaces. Furthermore, the plot of COPL vs CEPL reveals that original porosity decreased by compaction is greater in contrast to cementation (Fig. 18A, B). Cementation can induce a reduction of about 8.6% of the primary intergranular volume of the reservoirs averagely, and the porosity in about 85% of the reservoirs is affected more by compaction in contrast to cementation (Fig. 18B), revealing that compaction is the main cause for porosity loss.

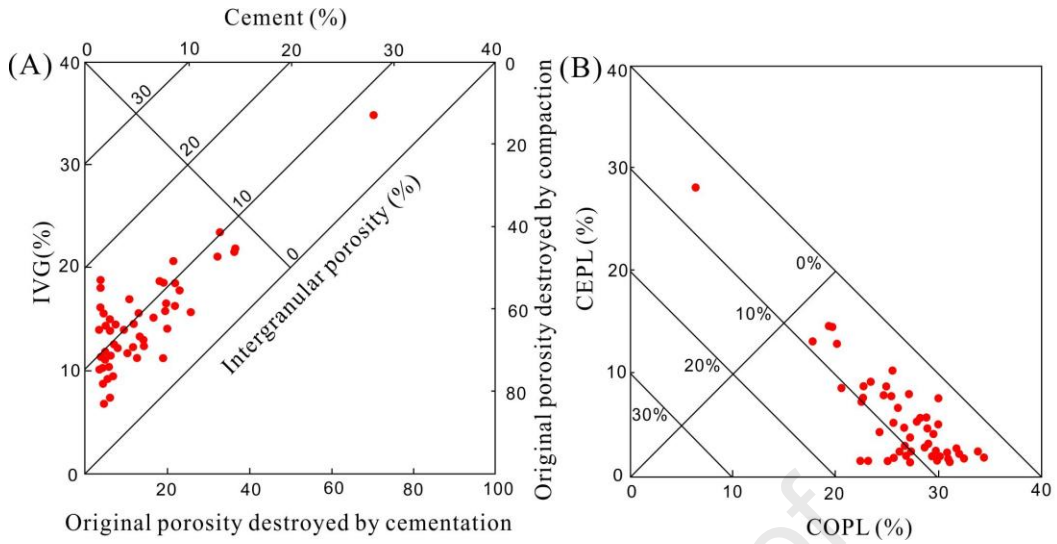

Fig. 18 (A) Crossplot of intergranular volume vs cement; (B) crossplot of the cementation porosity loss vs compaction porosity loss (after Ehrenberg, 1995 and 1989).

5.2.2 Cementation

The cement types in the BF, which primarily consist of calcite, quartz, and clay minerals like kaolinite and illite-smectite mixed-layer, account for less than 15% of the mineral composition. The role of cementation in pore reduction of the conglomerate reservoir is weaker than compaction (Fig. 18). Besides, the content of cement is significantly negatively correlated with the content of the argillaceous matrix (Fig. 19A), indicating that the content of the argillaceous matrix can be employed to roughly reflect the cementation intensity. Fig. 19B and C show that the amount of carbonate cement has an obvious negative association with permeability and porosity, which further demonstrates that carbonate cement occupies the pore space and deteriorates petrophysical properties. It's noteworthy that when the amount of carbonate cement is below 2.6%, the porosity and permeability were not appreciably affected. This may be attributed to a certain pore preservation effect by carbonate cement, which preserves the primary intergranular pores through anti-compaction and restraining the overgrowth of quartz.

There exists a complex relationship between reservoir petrophysical properties within different clay minerals (Fig. 19D-H). The clay fraction (<2 mm) from XRD data indicated that the clay minerals, which appeared in the pores in the form of pore-filling, pore-lining, or pore-

bridging, account for approximately 12.6% of the reservoir in the BF. In general, the more the total amount of clay minerals, the worse the petrophysical attributes (Fig. 19D). Interestingly, a positive association exists between kaolinite and porosity (Fig. 19E). This is mainly because the worm-shaped kaolinite aggregates formed soon after the dissolution of feldspar (Er et al., 2022). Moreover, in contrast with other clay minerals, kaolinite has a weaker ion exchange capacity, which enables the surface of the particle easily form a layer of oil film, thus making it lipophilic (Meng et al., 2020). Therefore, oil and gas tend to accumulate in kaolinite-rich reservoirs, concurrently inhibiting the compaction and carbonate cementation to a certain extent. Fig. 19F shows that the oil saturation in the reservoir increases in proportion to relative kaolinite content. As the content of chlorite goes up, the porosity increases slightly (Fig. 19G). Under SEM microscope, chlorite typically exhibited a leaf-shaped form in the reservoir, wrapping the particle surface as chlorite coatings, which are vital for the preservation of primary intergranular pores via restraining the overgrowth of quartz. The filamentous illite and illite-smectite mixed-layer has resulted in the division of large pores into small pores or micropores, occupying the pore space and reducing the petrophysical properties (Fig. 19H)

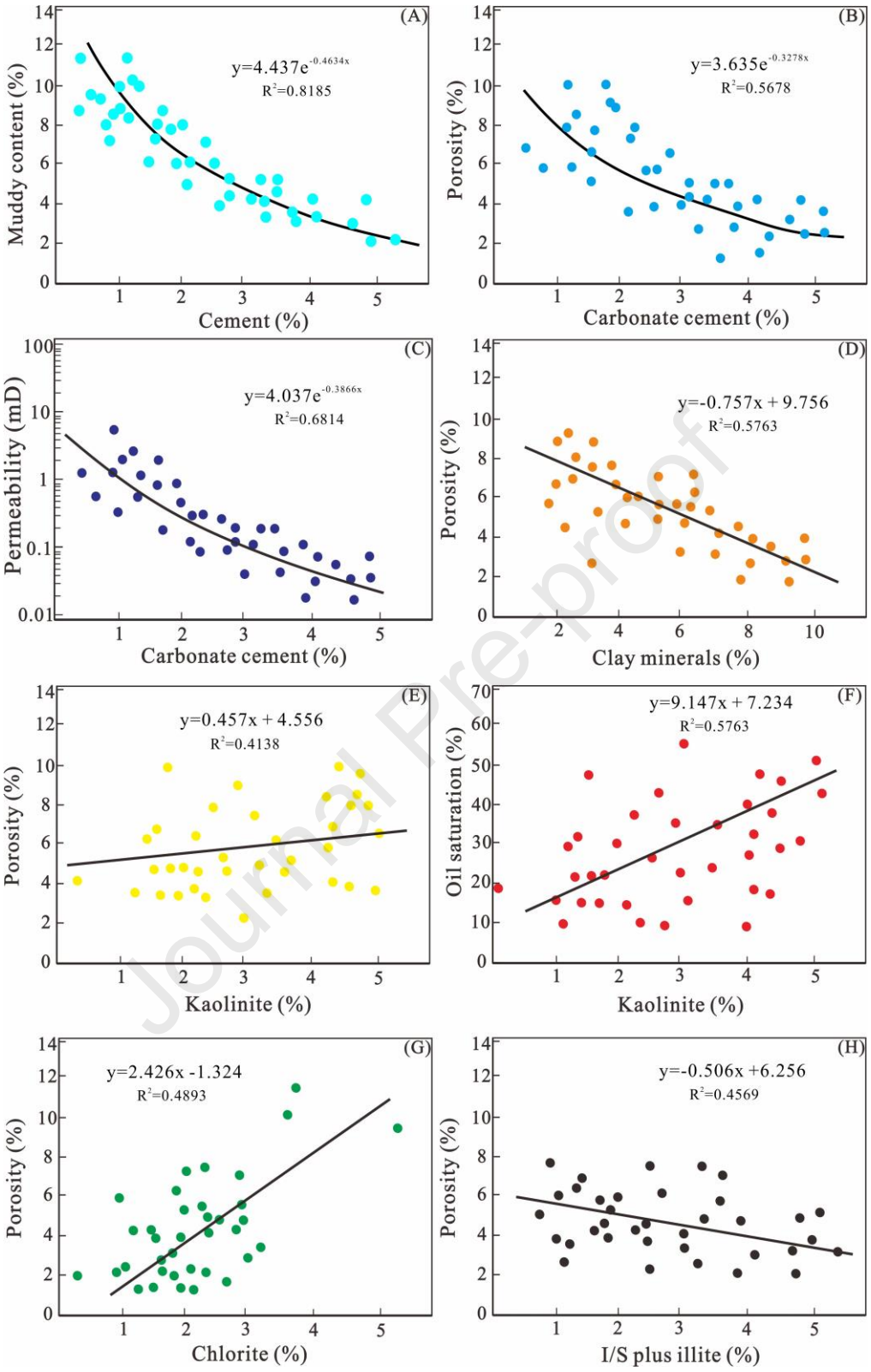

Fig. 19 (A) Crossplot of muddy content vs cement; (B) crossplot of carbonate cement vs porosity; (C) crossplot of carbonate cement vs permeability; (D) crossplot of clay minerals vs porosity; (E) crossplot of kaolinite vs porosity; (F) crossplot of kaolinite vs oil saturation; (G) crossplot of chlorite vs porosity; (H) crossplot of I/S plus illite vs porosity;

5.2.3 Dissolution

The dissolution of unstable components happens when provided with appropriate pore fluid, environmental medium, and diagenetic temperature (Kang et al., 2019). The dissolution minerals within the research region include carbonate cement, feldspar, and volcanic rock debris. The relationship between the areal porosity of dissolution and reservoir petrophysical properties of the BF in the Mahu Sag shows that when the areal porosity of dissolution is 1.5% ~ 2.2%, the total porosity does not increase obviously, that is, dissolution pores do not contribute significantly to the total porosity (Fig. 20A). However, the total porosity gradually increases while the areal porosity of dissolution reaches 2.2% ~ 3.1% (Fig. 20A). The porosity increases noticeably when the areal porosity of dissolution exceeds 3.2%, implying that the areal porosity of dissolution greatly improves the total porosity in this interval (Fig. 20A). Fig. 20B shows that no evident association exists between the areal porosity of dissolution and permeability, indicating that the dissolution does not significantly improve the permeability of the reservoir in the BF. This may be because the dissolution has primarily generated intragranular pores by partial dissolution of feldspar and rock debris particles with strong heterogeneity and poor connectivity, which increase the reservoir pore volume but do not correspondingly enhance the seepage capacity.

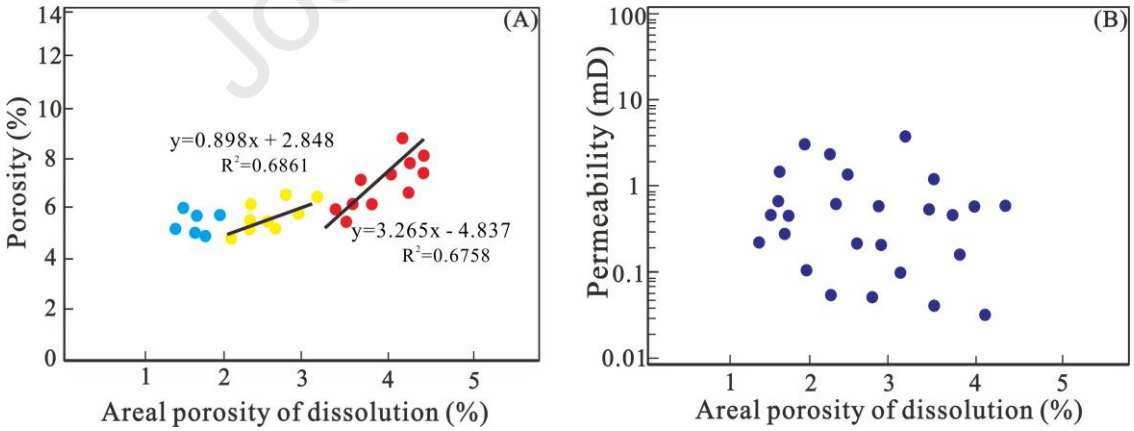

Fig. 20 (A) Crossplot of areal porosity of dissolution vs porosity; (B) crossplot of areal porosity of dissolution vs permeability.

5.3 Diagenetic Evolution Model

After the impacts of sedimentation and diagenesis on reservoir quality have been studied, the diagenetic evolution model within different lithofacies in the BF of the Mahu sag is established in Fig. 21. The medium-grained conglomerate reservoirs with high clay amount and poor sorting, which are primarily developed in the fan delta plain or debris flow, have undergone fast and intense compaction shortly after the deposition. The early argillaceous cementation is well developed, whereas carbonate and zeolite cements are less observed. Semi-plastic volcanic rock debris and feldspar particles exhibit linear or even concave-convex contact. These lithofacies have the worst reservoir quality with an average porosity of 4.2%, and no hydrocarbon is recorded (Fig. 21A). Their reservoir quality is thought to be governed by compaction, which has severely destructed the primary intergranular pores after deposition. Nevertheless, part of these reservoirs experienced late dissolution during mesodiagenesis, enhancing the petrophysical properties thus the second phase of hydrocarbon charging occurred in dissolution pores (Fig. 21B). Although considerable pores are produced, Large-scale fracturing is the premise and an effective approach to improving seepage capacity and productivity. Well-sorted fine-grained conglomerates with well-developed primary intergranular pores experienced complicated diagenetic histories (Fig. 21C–E). These reservoirs were primarily distributed in the subaqueous distributary channels and underwent compaction, early carbonate cementation, quartz overgrowth, chlorite coatings, and feldspar dissolution in the eodiagenesis posterior to deposition. Subsequently, the selective first period of hydrocarbon charging altered the diagenetic evolution process. Reservoirs without the first period of hydrocarbon charging were tightly compacted with relatively intense dissolution and slight carbonate cementation, where the second phase of hydrocarbon charging occurred in the dissolution pores (Fig. 21C). Similarly, these reservoirs have approximate petrophysical properties with medium conglomerates that have experienced late dissolution. Reservoirs with the first period of hydrocarbon charging are thought to have retarded the compaction degree. Resultantly, these reservoirs experienced later dissolution and a selective second period of hydrocarbon charging. Reservoirs with the second period of hydrocarbon charging possess the

highest oil saturation (Fig. 21E), which are considered the optimal petroleum exploration targets, whereas those without the second period of hydrocarbon charging are featured by late carbonate cementation and authigenic clay minerals (Fig. 21D). For those reservoirs, rational exploitation with natural energy is usually adopted for oil yielding because of the existence of primary intergranular pores, which considerably enhance the seepage capacity.

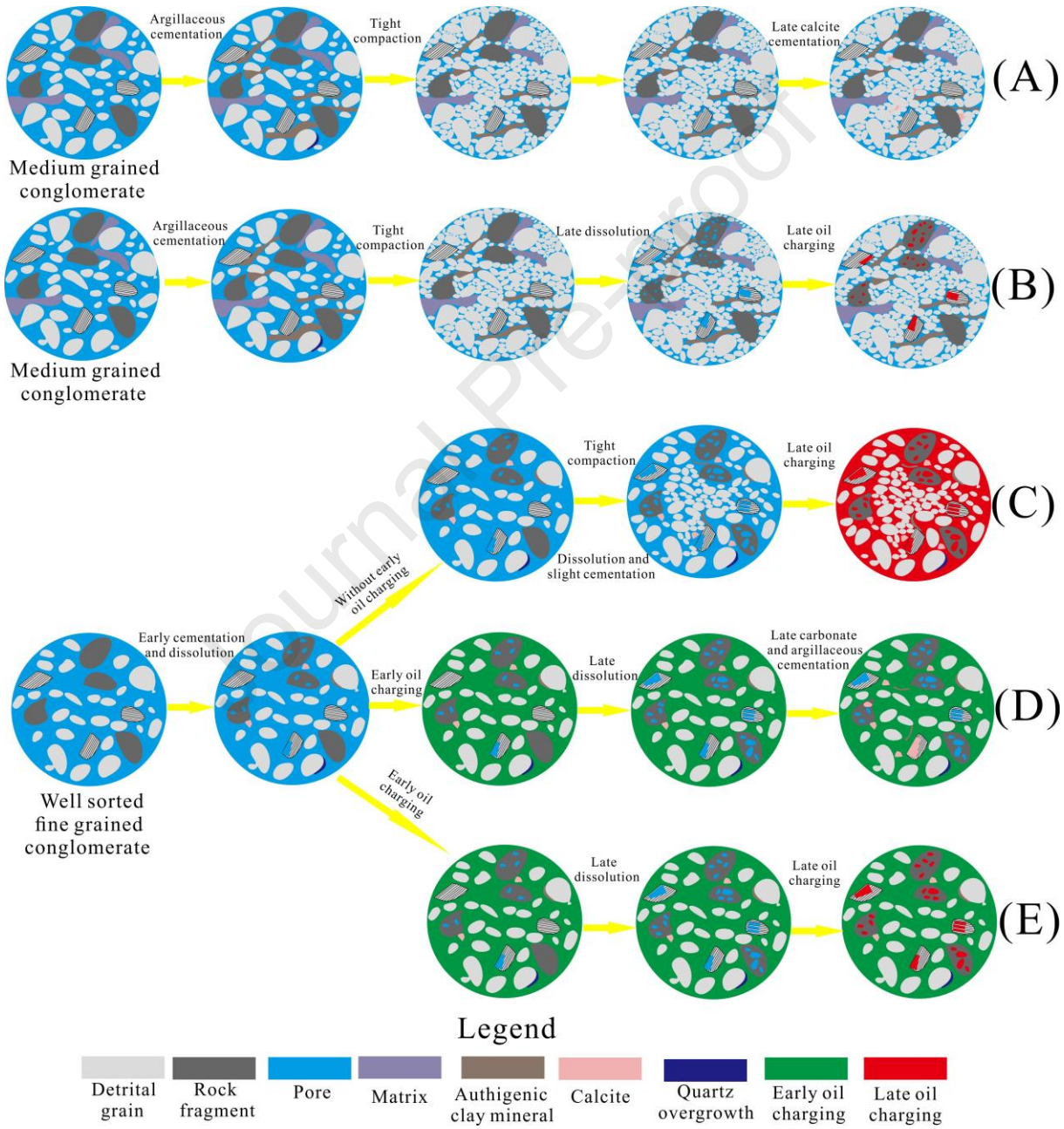

Fig. 21 Schematic diagram presenting the diagenetic evolutionary process of conglomerate reservoirs in the BF of the Mahu sag.

6. Conclusions

We performed a study to analyze the impacts of sedimentary and diagenetic processes on reservoir quality of conglomerate reservoirs developed in terrestrial lacustrine fan delta deposits by employing a series of techniques. The conclusions drawn from the current research are stated below:

Generally, sedimentary processes have a remarkable control on facies distribution, grain size, and clay content, causing the spatial variation of reservoir quality within the fan delta deposits. The fan delta plain is predominated by the offloading of debris flow deposits near provenance. The coarser grain and high clay content fraction at the base of gravity flow will first settle, whereas the finer grains at the top of flows progressively deposit in the fan delta front areas. From proximal to distal fan delta, a progressive conversion from cohesive muddy debris flow into traction current can be inferred from the variations of lithofacies associations. A total of 8 types of microfacies were identified where the conglomerates of the BF were deposited based on core descriptions, sedimentary structure, and wireline log responses. The lithofacies vary significantly among these microfacies in terms of their pore types, porosity, and permeability, which macroscopically restrict the distribution of high-quality reservoirs. In conclusion, the grayish-green fine-grained conglomerates concentrated in the subaqueous distributary channels provide the best reservoir performance because of their fine grain size, low clay content, and highly connected level of pore-throat. The braided river channels and mouth bars possess moderate reservoir quality compared with the subaqueous distributary channels. The debris flow deposits dominated by muddy debrites occupy the worst reservoir quality because of their highest clay content and coarsest grain size, causing the primary intergranular pores being hardly preserved.

The lacustrine fan delta conglomerate reservoirs have experienced intricate diagenetic alterations which involve physical compaction that continued throughout the entire burial, two phases of quartz cementation, dissolution of unstable components, early and late carbonate cementation, precipitation of authigenic clay minerals, and two phases of hydrocarbon charging. The compaction degree is closely tied to the content of the argillaceous matrix, which can

inhibit the development of carbonate cement and has relatively good lubrication thereby enhancing the destructive force of mechanical compaction. The role of cementation in pore reduction is weaker than compaction, which can be inferred from the plot of COPL versus CEPL. Nevertheless, an intricate association exists between reservoir petrophysical attributes within different clay minerals. A positive association exists between kaolinite and porosity due to their high correlation with the dissolution of unstable components. As the content of chlorite goes up, the porosity increases slightly because of the chlorite coatings, which preserve the primary intergranular pores by restraining the overgrowth of quartz cement. Filamentous illite and illite-smectite mixed-layer have resulted in the division of large pores into small pores or micropores, occupying the pore space thereby lowering the petrophysical attributes. Dissolution does not significantly contribute to permeability because partial dissolution commonly generated intragranular pores with strong heterogeneity and poor connectivity.

The formation of high-quality reservoirs in the BF is generally affected by sedimentary microfacies, compaction resistance capability, dissolution of unstable components, as well as oil charge. The most favorable reservoirs occur primarily in the subaqueous distributary channels in the fan delta front. These lithofacies are well-sorted fine-grained conglomerates with well-developed primary intergranular pores and secondary dissolution pores and have undergone two phases of oil charge. The second favorable petroleum target is the well-sorted fine-grained conglomerates which have undergone only one phase of oil charging. Reservoirs without the first period of hydrocarbon charging underwent relatively intense dissolution and slight carbonate cementation, and the late oil charging occurred in the dissolution pores, whereas those with the first period of hydrocarbon charging are featured by late carbonate cementation and precipitation of authigenic clay minerals. The results of this study may provide guidance for hydrocarbon exploration of fan delta systems and regions which have encountered similar sedimentary and diagenetic processes.

Author contribution

Zhichao Yu: Conceptualization, Methodology, Writing - original draft, Writing-review and editing. Zhizhang Wang: Project administration, Supervision. Wentian Fan: Formal analysis, Jie Wang: Formal analysis, Ziyan Li: Formal analysis.

Declaration of competing interest

The authors declare that they have no known competing financial interests or personal relationships that could have appeared to influence the work reported in this paper.

Acknowledgments

This study was supported by the Strategic Cooperation Technology Projects of CNPC and CUPB (Grant No. ZLZX2020-01). We are deeply grateful to the Exploration and Development Research Institute of Xinjiang Oilfield, CNPC, for providing research data and publication permission. We thank the Editor and anonymous reviewers for their thorough and critical reviews and suggestions, which have significantly improved the quality of this paper.

References

Cao, Z., et al. Origin of different chlorite occurrences and their effects on tight clastic reservoir porosity [J]. Journal of Petroleum Science and Engineering, 2018, 160: 384-392.

Chong Feng, Dewen Lei, Jianhua Qu, Junzhou Huo. Controls of paleo-overpressure, faults and sedimentary facies on the distribution of the high pressure and high production oil pools in the lower Triassic Baikouquan Formation of the Mahu Sag, Junggar Basin, China, Journal of Petroleum Science and Engineering, 2019, 176, 232-248.

Ehrenberg, S. N. and H. Baek. Deposition, diagenesis and reservoir quality of an Oligocene reefal-margin limestone succession: Asmari Formation, United Arab Emirates [J]. Sedimentary Geology, 2019, 393-394.

Ehrenberg, S.N., 1989. Assessing the relative importance of compaction processes and cementation to reduction of porosity in sandstones: discussion1. AAPG Bulletin 73, 1274–1276.

885 Ehrenberg, S.N., 1995. Measuring sandstone compaction from modal analyses of thin sections:
886 how to do it and what the results mean. Journal of Sedimentary Research 2, 369–379.
887 Er, C., Zhao J, Li Y., 2022. Relationship between tight reservoir diagenesis and hydrocarbon
888 accumulation: An example from the early Cretaceous Fuyu reservoir in the Daqing oil
889 field, Songliao Basin, China. Journal of Petroleum Science and Engineering. 208, 109422.
890 Gier, S., Worden, R.H., Johns, W.D., Kurzweil, H., 2008. Diagenesis and reservoir quality of
891 Miocene sandstones in the Vienna Basin, Austria. Mar. Pet. Geol. 25, 681–695.
892 Gómez-Paccard M, López-Blanco M, Costa E, et al. Tectonic and climatic controls on the
893 sequential arrangement of an alluvial fan/fan-delta complex (Montserrat, Eocene, Ebro
894 Basin, NE Spain) [J]. Basin Research, 2012, 24(4): 437-455.
895 Griffiths, J., et al. Origin and distribution of grain-coating and pore-filling chlorite in deltaic
896 sandstones for reservoir quality assessment [J]. Marine and Petroleum Geology, 2021, 134.
897 Grigsby, J.D., 2001. Origin and growth mechanism of authigenic chlorite in sandstones of the
898 lower Vicksburg Formation, South Texas. J. Sediment. Res. 71, 27–36.
899 Guo, P, et al. Controlling factors of high-quality hydrocarbon source rocks developed in
900 lacustrine shallow-water zone of the Junggar Basin, northwestern China [J]. AAPG
901 Bulletin, 2021, 105(10): 2063-2092.
902 Holmes A. Principles of physical geology [M]. London: Nelson, 1965.
903 Jia H B, Ji H C, Li X W, et al. A retreating fan-delta system in the Northwestern Junggar Basin,
904 northwestern China Characteristics, evolution and controlling factors [J]. Journal of Asian
905 Earth Sciences, 2016, 123: 162-177.
906 Jin J, Kang X, et al., 2017. Diagenesis and its influence on coarse clastic reservoirs in the
907 Baikouquan Formation of western slope of the Mahu Depression, Junngar Basin. Oil ＆
908 Gas Geology. 38 (2), 324-332 (in Chinese).
909 Jin Jun, Kang Xun, et al. Diagenesis and its influence on coarse clastic reservoirs in the
910 Baikouquan Formation of western slope of the Mahu Depression, Junngar Basin [J]. Oil
911 ＆ Gas Geology, 2017, 38(2):324-332.

912 Jin P.P., Ou C.H., et al., 2018. Evolution of montmorillonite and its related clay minerals and
913 their effects on shale gas development. Geophysical Prospecting for Petroleum. 57(3),
914 345-354 (in Chinese).
915 Kang X, Hu W X, Cao J, et al. Controls on reservoir quality in fan-deltaic conglomerates ：
916 Insight from the Lower Triassic Baikouquan Formation, Junggar Basin, China [J]. Marine
917 and Petroleum Geology, 2019, 103: 55-75.
918 Kra, K. L., et al. Sedimentological and diagenetic impacts on sublacustrine fan sandy
919 conglomerates reservoir quality: An example of the Paleogene Shahejie Formation (Es4s
920 Member) in the Dongying Depression, Bohai Bay Basin (East China) [J]. Sedimentary
921 Geology, 2022, 427.
922 Li J., Tang Y., Wu T., 2020. Overpressure origin and its effects on petroleum accumulation in
923 the conglomerate oil province in Mahu Sag, Junggar Basin, NW China. Petroleum
924 Exploration and Development. 47 (4), 726-739. https://doi.org/10.1016/S1876-
925 3804(20)60088-X.
926 Li, K., et al. Chlorite authigenesis and its impact on reservoir quality in tight sandstone
927 reservoirs of the Triassic Yanchang formation, southwestern Ordos basin, China [J].
928 Journal of Petroleum Science and Engineering, 2021, 205.
929 Meng W, Niu Z.C., et al., 2020. Genesis of authigenic kaolinite and its indicative significance
930 to secondary pores in petroliferous basins: A case study in the Dongying Sag, Bohai Bay
931 Basin, Eastern China. Journal of Petroleum Science and Engineering. 186, 106698,
932 https://doi.org/10.1016/j.petrol.2019.106698.
933 Molenaar, N., et al. Illite and chlorite cementation of siliciclastic sandstones influenced by clay
934 grain cutans [J]. Marine and Petroleum Geology, 2021, 132.
935 Pan, J., et al. Origin and charging histories of diagenetic traps in the Junggar Basin. AAPG
936 Bulletin, 2021, 105(2), 275-307.
937 Qingping Jiang, Chuixian Kong, et al. Sedimentary Characteristics and Evolution Law of a
938 Lacustrine Large-scale Fan Delta: A case study from the Triassic Baikouquan Formation

on the west slope of Mahu Sag [J]. Acta Sedimentologica Sinica, 2020, 38(05): 923-932. DOI:10.14027/j.issn.1000-0550.2019.089.

SHAN X, ZOU Z W, MENG X C, et al. Provenance analysis of Triassic Baikouquan Formation in the area around Mahu Depression, Junggar Basin [J]. Acta Sedimentologica Sinica, 2016, 34(5): 930-939.

TAN K J, WANG G D, LUO H F, et al. Reservoir characteristics and controlling factors of the Triassic Baikouquan Formation in Mahu slope area, Junggar Basin [J]. Lithologic Reservoirs, 2014, 26(6): 83-88.

Tang Yong, Yin Taiju, Qin Jianhua et al. Development of large-scale shallow-water fan delta: Sedimentary laboratory simulation and experiments [J]. Xinjiang Petroleum Geology 2017, 38(3): 253-263.

Warnecke, M., Aigner, T., 2019. Influence of subtle paleo-tectonics on facies and reservoir distribution in epeiric carbonates: integrating stratigraphic analysis and modeling (U. Muschelkalk, SW Germany). Sediment. Geol. 383, 82–100. https:// doi.org/10.1016/j.sedgeo.2019.01.015.

Wenbin Tang, Yuanyuan Zhang, Georgia Pe-Piper. Permian to early Triassic tectono-sedimentary evolution of the Mahu sag, Junggar Basin, western China: sedimentological implications of the transition from rifting to tectonic inversion, Marine and Petroleum Geology, 2021, 123, 104730, https://doi.org/10.1016/j.marpetgeo.2020.104730.

Wheatley, D., et al. Sedimentology, diagenesis, and reservoir characterization of the Permian White Rim Sandstone, southern Utah: Implications for carbon capture and sequestration potential [J]. AAPG Bulletin, 2020, 104(6): 1357-1373.

Wilson, R. D., et al. Evaluating the depositional environment, lithofacies variation, and diagenetic processes of the Wolfcamp B and lower Spraberry intervals in the Midland Basin: Implications for reservoir quality and distribution [J]. AAPG Bulletin, 2020, 104(6): 1287-1321.

965 Wu, W., et al. Seismic sedimentology, facies analyses, and high-quality reservoir predictions
966 in fan deltas: A case study of the Triassic Baikouquan Formation on the western slope of
967 the Mahu Sag in China's Junggar Basin. Marine and Petroleum Geology, 2020, 120.
968 Xian, B., et al. Using of stratal slicing in delineating delta-turbidite systems in Eocene Dongying
969 depression, Bohai Bay Basin: Insights for the evolution of multi-source delta-turbidite
970 systems in a fourth order sequence. Journal of Petroleum Science and Engineering, 2018,
971 168, 495-506.
972 Xinchuan Lu, Dong Sun, Xiangyang Xie, Xin Chen, Shuncun Zhang, Shengyin Zhang,
973 Guoqiang Sun, Ji'an Shi. Microfacies characteristics and reservoir potential of Triassic
974 Baikouquan Formation, northern Mahu Sag, Junggar Basin, NW China, Journal of Natural
975 Gas Geoscience, 2019, 4(1), 47-62, https://doi.org/10.1016/j.jnggs.2019.03.001.
976 Xinchuan Lu, Dong Sun, Xiangyang Xie, Xin Chen, Shuncun Zhang, Shengyin Zhang,
977 Guoqiang Sun, Ji'an Shi. Microfacies characteristics and reservoir potential of Triassic
978 Baikouquan Formation, northern Mahu Sag, Junggar Basin, NW China, Journal of Natural
979 Gas Geoscience, 2019, 4(1), 47-62, https://doi.org/10.1016/j.jnggs.2019.03.001.
980 XU Z Y, WANG A, HAN C C, et al. Formation mechanism of high-quality sandy-conglomerate
981 reservoir of Triassic Karamay Formation in Mahu area [J]. Lithologic Reservoirs，2020,
982 32(3): 82-92.
983 Yao Zongquan, Yu Xinghe, Gao Yang, et al. Application of multiple seismic attributes
984 matching technology in mapping coarse-grain fan deposition: A case from Triassic
985 Baikouquan Formation member 2 in Ma 131 area [J]. Acta Sedimentologica Sinica, 2017,
986 35(2): 371-382.
987 Yu, Z., Wang, Z., et al., 2021. Volcanic lithology identification based on parameter-optimized
988 GBDT algorithm: a case study in the Jilin Oilfield, Songliao Basin, NE China. J. Appl.
989 Geophys. 194, 104443. https://doi.org/10.1016/j. jappgeo.2021.104443.
990 Yu, Z., Wang, Z., Wang, J., Li, Z., 2022. Subtle reservoirs and implications for hydrocarbon
991 exploration in terrestrial lacustrine fan-delta deposits: Insights from the Triassic

Baikouquan Formation, Mahu Sag, Junggar Basin, western China. Marine and Petroleum Geology. 142, 105730. doi:https://doi.org/10.1016/j.marpetgeo.2022.105730.

Yu, Zhichao, Wang, Zhizhang, et al., 2022. Analysis of Factors of Productivity of Tight Conglomerate Reservoirs Based on Random Forest Algorithm. ACS Omega, 7 (23), 20390-20404. DOI: 10.1021/acsomega.2c02546

Zhang S.C., Huang L.L., et al., 2018. Diagenetic Facies of Triassic Baikouquan Formation in Mabei Area, Junggar Basin. Acta Petrolei Sinica. 36(2), 355-365 (in Chinese).

Zhaohui Xu, Suyun Hu, Lu Wang, Wenzhi Zhao, Zhenglin Cao, Ruiju Wang, Shuyuan Shi, Lei Jiang. Seismic sedimentologic study of facies and reservoir in middle Triassic Karamay Formation of the Mahu Sag, Junggar Basin, China, Marine and Petroleum Geology, 2019, 107, 222-236, https://doi.org/10.1016/j.marpetgeo.2019.05.012.

Zhenglu Xiao, Shijia Chen, Chaowei Liu, Zixing Lu. Lake basin evolution from early to Middle Permian and origin of Triassic Baikouquan oil in the western margin of Mahu Sag, Junggar Basin, China: Evidence from geochemistry, Journal of Petroleum Science and Engineering, 2021, 203, 108612, https://doi.org/10.1016/j.petrol.2021.108612.

Zhu Ning, Cao Yingchang, et al. Diagenesis and physical properties evolution of sandy conglomerate reservoirs: A case study of Triassic Baikouquan Formation in northern slope zone of Mahu Sag [J]. Journal of China University of Mining & Technology, 2019, 48(5): 1102-1118.

Zhu S.F., Zhu X.M., Wang Y.B., et al., 2010. Dissolution characteristics and pore evolution of Triassic reservoir in Kebai area, northwestern margin of Junggar Basin. Acta Sedimentologica Sinica. 28 (3): 547-555 (in Chinese).

Zhu Shifa, Zhu Xiaomin, Wang Yibo, et al. Dissolution characteristics and pore evolution of Triassic reservoir in Kebai area, northwestern margin of Junggar Basin [J]. Acta Sedimentologica Sinica, 2010, 28(3): 547-555.

Zou Niuniu, Zhang Daquan, Shi Ji an, et al. Lithofacies classification of glutenite in the fan delta of the Mabei area in the northwestern Junggar Basin and its reservoir significance [J]. Acta Geologica Sinica, 2017, 91(2): 440-452.

ZOU Z W, LI H, XU Y, et al. Sedimentary characteristics of the Baikouquan Formation, Lower Triassic in the Mahu Depression, Junggar Basin [J]. Geological Science and Technology Information, 2015(2): 20-26.

- A series of techniques like petrographical analysis, cores description, wireline, XRD, SEM, and MICP are integrated to investigate the fan delta reservoirs.
- The depositional process and diagenesis are linked to forecast the spatial and temporal distribution of the high-quality reservoirs.
- The diagenetic evolutionary model of the fan delta deposits within different lithofacies in the Baikouquan Formation is established.
- The grain size and clay content are key factors governing reservoir quality.

Declaration of interests

☒ The authors declare that they have no known competing financial interests or personal relationships that could have appeared to influence the work reported in this paper.

☐The authors declare the following financial interests/personal relationships which may be considered as potential competing interests: